



# Effect of Divalent / Trivalent Doping on Structural, Electrical and Magnetic Properties of Spinel Ferrite Nanoparticles

Mahesh B. Khanvilkar,<sup>1,2,\*</sup> Arvind K. Nikumbh,<sup>1</sup> Ramdas A. Pawar,<sup>1</sup> Neeta J. Karale,<sup>1</sup> Pratik A. Nagwade,<sup>1</sup> Deepak V. Nighot,<sup>1</sup> Gulab S. Gugale,<sup>1</sup> Mohan D. Sangale,<sup>1</sup> Sham B. Misal<sup>1</sup> and Sharad P. Panchgalle<sup>2</sup>

## Abstract

Five nanosized divalent/trivalent doped spinel ferrites (a) Cu-Zn co-doped nickel ferrite ( $\text{Ni}_{0.6}\text{Cu}_{0.2}\text{Zn}_{0.2}\text{Fe}_2\text{O}_4$ ), (b) Cd-doped cobalt ferrite ( $\text{Co}_{0.9}\text{Cd}_{0.1}\text{Fe}_2\text{O}_4$ ), (c) Al-doped cobalt ferrite ( $\text{CoAl}_{0.3}\text{Fe}_{1.7}\text{O}_4$ ), (d) Ru-doped cobalt ferrite ( $\text{CoRu}_{0.04}\text{Fe}_{1.96}\text{O}_4$ ), and (e) Ni-doped gamma ferric oxide ( $\text{Fe}_{2.55}\text{Ni}_{0.12}\square_{0.33}\text{O}_4$ ; where  $\square$ , is Fe vacancy) are synthesized by coprecipitation method. Energy dispersive X-ray (EDS) and ICPE analysis confirm the stoichiometry of the elemental composition of the synthesized materials. The X-ray diffraction pattern (XRD) confirmed the cubic structure with enlarged lattice parameters as compared to undoped compounds. The size and crystalline structure are confirmed by scanning electron micrographs (SEM), transmission electron microscopy (TEM), and Histogram found approx. 18-52nm. Selected area electron diffraction (SAED) pattern exhibited the lattice planes which indicates the particle is crystalline in nature. Electrical conductivity, Seebeck voltage and Hall effect measurements for these samples showed n-type semiconductors. All samples show typical hysteresis behavior with a decrease in saturation magnetization, and an increase in coercivity as compared to respective undoped ferrites. The remanence ratio was found in the range of 0.11 to 0.47 indicating multi-domain structure for all samples except  $\text{Fe}_{2.55}\text{Ni}_{0.12}\square_{0.33}\text{O}_4$ , which have single domain structure ( $M_R/M_S=0.58$ ). The observed irreversibility of zero-field cooled (ZFC)-field cooled (FC) curve for  $\text{Fe}_{2.55}\text{Ni}_{0.12}\square_{0.33}\text{O}_4$ , is indicative of ferromagnetism.

**Keywords:** Nanosized doped spinel ferrites; Ferromagnetism; Electrical conductivity; Magnetization; Exchange interaction.

Received: 19 October 2022; Revised: 16 March 2023; Accepted: 19 March 2023.

Article type: Research article.

## 1. Introduction

In recent decades, the preparation and characterization of nanoparticles and nano-structured materials of various chemical compositions, structures, and morphologies have become a topic area in inorganic materials research. These issues have emerged in the development of nanotechnologies for manufacturing nanopowders for structural and functional applications. Magnetic nanoparticles, especially nanocrystalline spinel ferrites have across-the broad applications in medicine, photocatalysis, microwave devices, transformers, electric generators, storage instrumentations, multilayer chip inductors, ferrofluids, rod antenna, ferrite cores, humidity sensors, magnetic recorders, *etc.*<sup>[1-3]</sup> The spinel

ferrite has the general formula (A)[B<sub>2</sub>]O<sub>4</sub> that can be portrayed as a cubic closed pack of oxygen ions. The round brackets (A) represent tetrahedral interstitial sites and square brackets [B] corresponds to larger octahedral sites. Both of these sites are occupied by cations, with divalent ions occupying tetrahedral and trivalent ions occupying octahedral sites. The magnetic moments of the cations occupying octahedral lattice sites are oriented in the same direction, whereas the magnetic moments of the cations at tetrahedral sites are oriented antiparallel to that of the cations at octahedral sites. The resultant of these two magnetic moments gives rise to the net magnetization in spinel ferrite.

The unit cell of the spinel structure is obtained by doubling approximately face-centered cubic oxygen sublattices along each of the three directions. Of the resulting 64 tetrahedral (A) sites and 32 octahedral [B] sites, only 8 and 16 are occupied, respectively, by cations in stoichiometric spinel. Most spinel compounds belong to the space group Fd3m.<sup>[4]</sup>

<sup>1</sup> Department of Chemistry, Savitribai Phule Pune University (Formerly University of Pune), Ganeshkhind, Pune 411 007, India.

<sup>2</sup> K. M. C. College, Khopoli, Tal-Khalapur, Dist. Raigad – 410203, India.

\*Email: [mb.khanvilkar@gmail.com](mailto:mb.khanvilkar@gmail.com) (M. B. Khanvilkar)

Occupation of the tetrahedral sites entirely with a divalent metal ion produces a normal spinel structure, while the occupation of the octahedral site with the divalent metal ion yields an inverse spinel structure. If divalent metal ions are present on both (A) and [B] sublattices, the structure is of mixed or disordered spinel.<sup>[5]</sup> Information on cation distribution and spin alignment is essential to understand the magnetic properties of spinel ferrites. The interesting physical and chemical properties of ferrosinels arise from their ability to distribute the cations among the available tetrahedral (A) and octahedral [B] sites. The determination of cation distribution at the tetrahedral (A) and octahedral [B] sites have been the subject of many studies. X-ray diffraction, Mossbauer spectroscopy, Magnetization measurement, electron spin resonance (ESR), Neutron diffraction, Thermoelectric, and Nuclear magnetic resonance (NMR), Quantum mechanical method, and Rietveld refinement have been employed to determine the cation distribution in spinels.<sup>[5,6]</sup>

In recent decades, the doped metal ions can substitute either (A) site or [B] site or both depending upon its valency and site type, which in turn affects the structural, electrical, and magnetic properties of the spinel ferrites.<sup>[7]</sup> One of the difficulties regarding the crystal chemistry of spinel ferrites is determining the metal oxidation states and cation distribution among the tetrahedral (A) and octahedral [B] sites of the spinel structure. This determination becomes more complex when two or more metallic cations with relatively similar oxidation states share the lattice sites and which has been determined by X-ray photoelectron spectroscopy (XPS). Thermodynamic considerations have shown that trivalent or tetravalent cations are usually positioned on octahedral sites, while divalent have no preference.<sup>[8]</sup> The dependency of any particular doped composition adopting the normal, inverse, or mixed spinel structure lies in lattice energy, crystal field stabilization, and covalency effects. Similarly, the site preference for any particular dopant will arise from the balance of energy considerations. The ferrimagnetic properties of cobalt ferrite ( $\text{CoFe}_2\text{O}_4$ ) or nickel ferrite ( $\text{NiFe}_2\text{O}_4$ ) are closely related to the cation arrangements and oxidation states in the two crystallographic sites (*i.e.*, A and B sites) and are inverse spinel structures.<sup>[9]</sup> The antiferromagnetic properties of Zinc ferrite ( $\text{ZnFe}_2\text{O}_4$ ) or Cadmium ferrite ( $\text{CdFe}_2\text{O}_4$ ) are closely related to the cation arrangements and oxidation states in the same crystallographic site (*i.e.*, B-site), which are antiparallel and normal spinel.<sup>[10]</sup> The ferrimagnetic properties of gamma- $\text{Fe}_2\text{O}_3$  (maghemite) are believed to be close to that of  $\text{Fe}_3\text{O}_4$  (magnetite) and are inverse spinel structures, of which one-third of  $\text{Fe}^{3+}$  at the B-site is vacant. It is frequently written as  $(\text{Fe}^{3+})_A[\text{Fe}^{3+}_{5/3}\square_{1/3}]_B\text{O}_4^{2-}$ , where  $\square$  it stands for Fe vacancy.<sup>[11]</sup>

Most of the research is emphasized the modification of magnetic properties for a substitution or doped of  $\text{Fe}^{3+}$  ions for cobalt ferrites with transition metal ions (Mn, Cr, Cd, Ni, Zn, Ru, *etc.*) and rare-earth ions (Gd, Pr, Nd, Sm, *etc.*).<sup>[12-14]</sup> The electrical and magnetic properties of nonmagnetic  $\text{Al}^{3+}$  doped cobalt ferrites are also reported by various groups.<sup>[15]</sup> The effect of rare-earth ion doped on magnetization and initial permeability of Mn-Zn, Cu-Zn, Ni-Zn, Mg-Zn, and Ni-Cd ferrite systems have also been extensively studied.<sup>[16,17]</sup> The nano Cobalt ferrite ( $\text{CoFe}_2\text{O}_4$ ) particles are worthy contenders in the medical field for isolation and purification of genomic (DNA) and the separation of polymerase chain reaction (PCR) ready DNA and especially in hyperthermia treatment.<sup>[18]</sup> Mn-doped Co-Zn ferrites ( $\text{Co}_{0.6}\text{Zn}_{0.4}\text{Mn}_x\text{Fe}_{2-x}\text{O}_4$ ) and Cd-doped Co-Zn ferrites ( $\text{Co}_{0.5}\text{Zn}_{0.5}\text{Cd}_{1.5x}\text{Fe}_{2-x}\text{O}_4$ ) were synthesized by standard solid-state reaction method and electrical, magnetic, mechanical properties and photocatalytic degradation activities reported.<sup>[19]</sup> While nanosized doped-gamma ferric oxide has increased the coercivity and saturation magnetization to a large extent for its use in high-density recording disks or high-speed digital tape.<sup>[20]</sup> Structural and dielectric studies of Zn, Gd, and Ga doped  $\text{NiFe}_2\text{O}_4$  are synthesized by two different routes as solid-state reaction and citrate method.<sup>[21]</sup> The samples synthesized using solid-state reaction showed magnetic order, whereas the samples prepared through the citrate method exhibited super magnetic nature. From this literature, it is learned that the physical and chemical properties of spinel ferrites are strongly affected by synthesis conditions and methods as these influence the chemical composition, stoichiometry, point defect concentration (*i.e.*, dopants), and used in energy technology.<sup>[21]</sup>

With this view in mind, the doped spinel ferrites have attracted much interest due to their novel magnetic and electrical properties and are still the subject of much research aimed at a better understanding of the magnetic interaction between A site and B site. These properties are associated with the distribution and occupancy of cations in the spinel crystal structure. The aim for both divalent and/or trivalent dopants is with ionic radii comparable to that of  $\text{Fe}^{3+}$ . Hence they would be expected at different crystallographic sites (A or B sites) of spinel ferrites. Also, different substituting cations have their own preferential sites when doping in the spinel ferrites. When doping in the spinel ferrite phase by partial reduction of  $\text{Fe}^{3+}$  to  $\text{Fe}^{2+}$  took place, but overall charge neutralization, oxygen vacancies are created at the octahedral site, thus decreasing the electrical and magnetic parameters.

In general, the synthesis technique of spinel ferrite plays a vital role in determining the structural, electrical, and magnetic properties. The main novel synthesis methods of

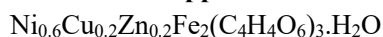
nanosized spinel ferrites are sol-gel, co-precipitation, oxidation, micro-emulsion, hydrothermal, spray pyrolysis, reverse micelles, and ultrasound-assisted synthesis.<sup>[3]</sup> In the present study, five nano-sized divalent and /or trivalent doped inverse spinel ferrites such as (a) Cu-Zn codoped nickel ferrite ( $\text{Ni}_{0.6}\text{Cu}_{0.2}\text{Zn}_{0.2}\text{Fe}_2\text{O}_4$ ), (b) Cd-doped cobalt ferrite ( $\text{Co}_{0.9}\text{Cd}_{0.1}\text{Fe}_2\text{O}_4$ ), (c) Al-doped cobalt ferrite ( $\text{CoAl}_{0.3}\text{Fe}_{1.7}\text{O}_4$ ), (d) Ru-doped cobalt ferrite ( $\text{CoRu}_{0.04}\text{Fe}_{1.96}\text{O}_4$ ), and (e) Ni-doped gamma ferric oxide ( $\text{Fe}_{2.55}\text{Ni}_{0.12}\square_{0.33}\text{O}_4$ ; where  $\square$  is a vacancy, it stands for Fe vacancy) were synthesized using tartrate / Succinate or hydroxide coprecipitation method (soft chemical route). This method is simple, low cost, exhibits high purity, and ability to produce a fine and homogeneous nano particle powder with any risk of contamination in shorted duration than other methods. This work aims to explain the effect of dopants on the structural, and electrical properties of the as-synthesized doped samples. The magnetic measurements are also undertaken to gain information about the cation distribution, and possible canted spin structures at both A and B sites in these doped inverse spinel ferrites.

## 2. Experimental

Nanoparticles of undoped and doped ferrites were synthesized by the coprecipitation method. All the reagents in this study were supplied by Sigma-Aldrich and were used without further purification.

### 2.1 Synthesis of tartrate/succinate and hydroxide precursors

#### 2.1.1 Nickel-copper-zinc-iron tartrate mono hydrate,



The tartrate precursor was prepared using stoichiometric amounts of  $\text{NiSO}_4 \cdot 6\text{H}_2\text{O}$  (1.9593 g),  $\text{CuSO}_4 \cdot 5\text{H}_2\text{O}$  (0.7110 g)  $\text{ZnSO}_4 \cdot 7\text{H}_2\text{O}$  (1.1154 g), and  $\text{FeSO}_4 \cdot 7\text{H}_2\text{O}$  (8.1267 g) dissolved in 100 mL double distilled de-ionized water. The solution was placed in a three-necked round bottom flask under a stream of dry nitrogen atmosphere and the solution was stirred on amagnetic stirrer with a hot plate. Then, the pH was adjusted to about 5.90 with dilute  $\text{H}_2\text{SO}_4$ . To this diammonium tartrate solution (8.7468 g dissolved in 40 mL double distilled water) was added drop by drop with stirring till a permanent precipitate occurred. Then acetone was added in equal amounts to get a more homogeneous, stoichiometric, fine-grained precursor powdered, and the resulting solution was digested at 50 °C for 30 minutes. The obtained precipitate was filtered and washed with double-distilled deionized water. The as-synthesized precipitate was air-dried at room temperature. The flow sheet diagram for Nickel-copper-zinc-iron tartrate monohydrate and subsequent conversion to

nanosized doped inverse spinel ferrites is depicted in Fig. S1 of the supplementary information file.

A similar procedure was used for the synthesis of (a) undoped nickel-iron and cobalt-iron tartrate, (b) Cadmium-cobalt-iron tartrate one and half hydrate ( $\text{Cd}_{0.1}\text{Co}_{0.9}\text{Fe}_2(\text{C}_4\text{H}_4\text{O}_6)_3 \cdot 1.5\text{H}_2\text{O}$ ), (c) Aluminium-cobalt-iron succinate seven hydrate ( $\text{Al}_{0.3}\text{CoFe}_{1.7}(\text{C}_4\text{H}_4\text{O}_4)_3 \cdot 7\text{H}_2\text{O}$ ), (d) Cobalt-ruthenium-iron tartrate mono hydrate ( $\text{CoRu}_{0.04}\text{Fe}_{1.96}(\text{C}_4\text{H}_4\text{O}_6)_3 \cdot \text{H}_2\text{O}$ ) by taking the stoichiometric amount of respective salts.

#### 2.1.2 $\gamma$ -Ferric-nickel oxy-hydroxide, ( $\gamma\text{-Fe}_{0.96}\text{Ni}_{0.04}\text{O}(\text{OH})$ )

The preparation of gamma-Ferric-Nickel oxy-hydroxide in a definite morphology is achieved by gas-liquid-solid phase reaction involving the oxidation of precipitated ferrous-nickel hydroxide by air.<sup>[22]</sup>

0.347g of iron metal powder was dissolved in 3mL of concentrated hydrochloric acid in a three-neck flask under the nitrogen atmosphere and evaporated slowly to obtain a green ferrous chloride. It was then dissolved in distilled water to make the volume 250 mL giving a 0.025M  $\text{FeCl}_2$  solution. From this, take 150 mL  $\text{FeCl}_2$  solution was mixed with 0.0446 g  $\text{NiCl}_2 \cdot 6\text{H}_2\text{O}$  and 100mL ammonium chloride solution (0.1M) and was introduced into a 500 mL three-neck flask. The solution was maintained at 50 °C. Air was introduced into the mixture at a rate of 500 mL  $\text{min}^{-1}$ . The hydrogen ion concentration of the solution was maintained at pH 6.00 by adding aqueous ammonia (0.1 M) drop wise from a separatory funnel. An addition of about 130 mL of aqueous ammonia (0.1M) during 2 h was required for the completion of the reaction. The yellowish-brown precipitate of  $\gamma$ -ferric oxy-hydroxide containing nickel was filtered through Whatman filter paper No.42 and washed thoroughly with distilled water till free from chloride. It was air-dried at the ambient temperature.

The same procedure was used for the synthesis of undoped gamma ferric oxide by taking 150 mL  $\text{FeCl}_2$  (0.025M) and 100 mL ammonium chloride (0.1M). Then add drop by drop 130 mL  $\text{NH}_4\text{OH}$  (0.1 M) over two h.

### 2.2 Synthesis of nanosized doped spinel ferrites

The above undoped and doped precursors except gamma ferric oxi hydroxide were calcined slowly at 700 °C for two hours in a platinum crucible under a normal air atmosphere. This sample was then reground and recalcined at the same temperature for another 2h. The obtainable doped spinel ferrites such as  $\text{Ni}_{0.6}\text{Cu}_{0.2}\text{Zn}_{0.2}\text{Fe}_2\text{O}_4$ ,  $\text{Cd}_{0.1}\text{Co}_{0.9}\text{Fe}_2\text{O}_4$ ,  $\text{Al}_{0.3}\text{CoFe}_{1.7}\text{O}_4$ ,  $\text{CoRu}_{0.04}\text{Fe}_{1.96}\text{O}_4$  and undoped samples such as  $\text{NiFe}_2\text{O}_4$  and  $\text{CoFe}_2\text{O}_4$  were restored in a desiccator.

The nickel-containing gamma ferric oxy-hydroxide and undoped gamma ferric oxy-hydroxide ( $\gamma$  FeOOH) was placed in a platinum boat and kept in a tubular furnace. The sample was heated at a constant temperature of 250 °C in the air. After one hour, the sample was reground and reheated at the same temperature yielding reddish-brown nickel doped and undoped gamma ferric oxide.

### 2.3 Characterization Technique

Precursors were characterized at the first stage of carbon and hydrogen by the microanalytical technique. The composition of metals in the precursors and doped spinel ferrites was carried out by inductively coupled plasma spectrometer (ICPES) (ICP-AES instrument ARCOS from M/S. Spectro Germany) and Energy dispersive X-ray analysis (EDS) on PHILIPS XL 30 CP instrument. The infrared spectra of compounds were carried out with Perkin-Elmer 1600 series FTIR spectrophotometer on KBR pellets. The thermal behavior (TGA and DTA) of the precursors was conducted on Mettler Toledo 850 instrument. The crystal structure was characterized by X-ray diffraction (XRD) carried out using a Siemens D 500 diffractometer with  $\text{CuK}\alpha$  radiation ( $\lambda = 1.5418 \text{ \AA}$  and  $\theta = 20 - 80^\circ$ ) at room temperature. Philips 30 XL FEG scanning electron microscope (SEM) was used to examine the surface morphology and particle size distribution of prepared doped spinel ferrites. The morphology and the size of resultant powders were obtained by Transmission electron microscopy (TEM) and corresponding selected area electron diffraction (SAED) pattern on a JEOL-2010 transmission electron microscope, operating at an accelerating voltage of 208 kV. (The TEM specimen of doped spinel ferrites was prepared from the dispersed by dispersing in 2-propanol and ultrasonicated. Then, one or two drops of the mixed solution were cast on an amorphous carbon film-coated copper TEM grid). The electrical conductivity, Seebeck voltage (*i.e.* thermoelectric voltage), and Hall effect measurements were performed similarly to describe in the literature.<sup>[12,23]</sup> For Seebeck voltage measurements, the sample in the form of a pellet of 10 mm thickness was pressed between two platinum discs fixed at the ends of two ceramic blocks. One of these blocks was spring-loaded two obtained good pressure contact. This sample holder along with the sample was placed in a constant temperature zone of a furnace, whose temperature was held to within  $\pm 1^\circ\text{C}$ . The temperature of the ends of the sample was measured with chrome-alumini thermocouples, placed in such a way as to touch the sample ends. These junctions were as to touch the sample ends. These junctions were insulated from platinum disks and ceramic blocks by means of thin mica sheets. During the measurements, the

sample was equilibrated at each temperature for about 10 mins. Temperature differences of 2 to 20°C were used along the sample. The thermoelectric voltage (or Seebeck voltage) developed across the sample and the temperature of the sample ends were read on a Philips PP 9004 micro voltmeter. A set of the values of thermoelectric voltage at various temperatures thus obtained ( $\mu\text{V K}^{-1}$ ) was plotted against the respective absolute temperatures, T (K). The predominant charge carriers in a temperature gradient diffuse towards the cold end of the sample. The sign of the probe at the lower temperature is the sign of the Seebeck voltage or thermoelectric voltage. The dielectric measurement was carried out at room temperature using HIOKI model 3532-50 LCR Hi Tester (frequency range from 100 Hz to 5 MHz).

The magnetic behavior of the samples was investigated using a SQUID magnetometer (Quantum Design MPMS-55). The sample magnetization was carried out in a field of 100 Oe on warming through the temperature range  $5 < T \text{ (K)} < 325$  after cooling the sample both in the measuring field (field cooling-FC) and in the absence of an applied field (zero-field cooling - ZFC). The magnetic hysteresis measurement was also studied at room temperature by using a vibrating sample magnetometer (PAREG and G model no.4508) with an applied field up to 20 k Oe. The saturation magnetization ( $M_s$ ) and coercivity were determined from the hysteresis loop.

## 3. Results and discussion

### 3.1 Characterization of precursors

Mixed metal tartrate/succinate and hydroxide precursors were obtained by the reaction of stoichiometric respective metal salt in an aqueous solution with slow addition of 3% ammonium dicarboxylate or ammonium hydroxide. The optimum conditions such as the pH, solution temperature, precipitate age time, and stirring were chosen. Similarly, for stoichiometric precipitation of tartrate or succinate precursors along with an equal amount of distilled acetone, digested for half an hour to get the complete precipitation under controlled stirring. The composition of the dicarboxylate and hydroxide precursors such as C and H was carried out by a microanalytical technique, while metal analysis was carried out by the inductively coupled plasma spectrometer (ICPES). The observed compositions are summarized in Table T1 of the supplementary information file. They are found to be within  $\pm 0.5\%$  of the calculated values. The results showed a close relationship with the nominal compositions of the precursors. The presence of water in the crystallization of these compounds was confirmed based on the thermal analysis curve. These results are also further supplemented by the infrared spectral data.

The infrared spectrums of these precursors (Figures are not shown) showed the band at  $3443\text{ cm}^{-1}$  corresponds to the  $\nu$  (O-H) vibration of water. The width of this band confirms the presence of intramolecular hydrogen bonds in these compounds.

The band at  $1750\text{ cm}^{-1}$  in the infrared spectra of d-tartaric acid/succinic acid assigned to  $\nu$  (C = O) is replaced in the tartrate/succinate complex (*i.e.*, precursor) spectra by the bands;  $\nu_{\text{asy}}$  (OCO) at  $1593\text{ cm}^{-1}$  and  $\nu_{\text{sy}}$  (C = O) at  $1415 - 1367\text{ cm}^{-1}$ . The presence of these two bands in the infrared spectra for tartrate/succinate precursor suggests the coordination of both  $\text{COO}^-$  groups present in the tartaric acid/succinic acid molecule to the metallic ions. Infrared spectral analysis showed bidentate linkage to be more favorable for tartrate/succinate precursor due to the difference between the stretching vibration of antisymmetric and symmetric (C = O) groups. The infrared spectra in the range  $1177 - 1001\text{ cm}^{-1}$  do not show any significant differences between tartaric acid / succinic acid and the mixed-metal complexes (*i.e.*, precursor). From these, it concludes that there is no bonding with the free C – OH group to the metal in a solid state.<sup>[24]</sup> Other bands, which are all combination bands, may be assigned to the different normal modes of vibrations of the carboxylate group. The  $\nu$  (M – O) vibrations have been identified for these precursors. Water molecules present in all precursors constitute only water of hydration and do not coordinate with the metal ions. These dicarboxylate/hydroxide precursors have a magnetic moment (by Faraday's Technique) in the range of 6.78 to 9.17 B.M. for all precursors (see Table T1 of supplementary information file). These magnetic moments ( $\mu$ ) at room temperature showed slightly less value than the theoretical ones in all compounds. These differences may be due to the antiferromagnetic interaction between the odd electrons of two or more paramagnetic metallic ions. All the precursors were isolated as a powder and not as a single crystal, meaning that no complete structural determination can be made. However, the infrared spectrum and magnetic susceptibility measurements suggested a chain-like polymeric octahedral structure of the precursors.<sup>[25]</sup>

The TGA and DTA curve for tartrate/succinate and hydroxide precursors such as (a)  $\text{Ni}_{0.6}\text{Cu}_{0.2}\text{Zn}_{0.2}\text{Fe}_2(\text{C}_4\text{H}_4\text{O}_6)_3 \cdot \text{H}_2\text{O}$ , (b)  $\text{Co}_{0.9}\text{Cd}_{0.1}\text{Fe}_2(\text{C}_4\text{H}_4\text{O}_6)_3 \cdot 1.5\text{H}_2\text{O}$ , (c)  $\text{Al}_{0.3}\text{CoFe}_{1.7}(\text{C}_4\text{H}_4\text{O}_4)_3 \cdot 7\text{H}_2\text{O}$ , (d)  $\text{CoRu}_{0.04}\text{Fe}_{1.96}(\text{C}_4\text{H}_4\text{O}_6)_3 \cdot \text{H}_2\text{O}$ , (e)  $\gamma\text{-Fe}_{0.96}\text{Ni}_{0.04}\text{O}(\text{OH})$  were recorded under normal air atmosphere and is shown in Fig. S2 of the supplementary information file. The representative of TGA and DTA curve for  $\text{Ni}_{0.6}\text{Cu}_{0.2}\text{Zn}_{0.2}\text{Fe}_2(\text{C}_4\text{H}_4\text{O}_6)_3 \cdot \text{H}_2\text{O}$  is shown here in Fig. 1. The dehydration of this precursor can be detected on the DTA curve at  $\sim 150^\circ\text{C}$ .

The TGA curve shows weight loss for dehydration step up to  $180^\circ\text{C}$  corresponds to the loss of all water molecules (see eq. 1). The isothermal heating of the sample under normal air at  $160^\circ\text{C}$ , the infrared spectrum showed the absence of the –OH band and a considerable decrease in the intensity as compared to parent tartrate precursor. The observed mass loss and corresponding temperature ranges are shown in Table T2 of the supplementary information file. The oxidative decomposition of these precursors was indicated by the presence of strong and broad exothermic peaks on the DTA curve at around  $250^\circ\text{C}$  corresponds to the formation of the final oxide. The TGA curve showed one-step weight loss in the temperature range of  $180 - 500^\circ\text{C}$ , corresponding to the formation of Cu-Zn codoped nickel ferrite (see Table T2). In the isothermally heated sample at around  $400^\circ\text{C}$ , the infrared spectrum showed a band at  $2365\text{ cm}^{-1}$ , indicating the presence of entrapped carbon dioxide, *i.e.*, adsorbed  $\text{CO}_2$  is present in the final residue (see Eq. 2). The powdered XRD gave a slightly broad peak at a similar position of nickel ferrite. This entrapped  $\text{CO}_2$  can be removed by heating the residue at  $700^\circ\text{C}$  for 2hr (see Eq. 3).

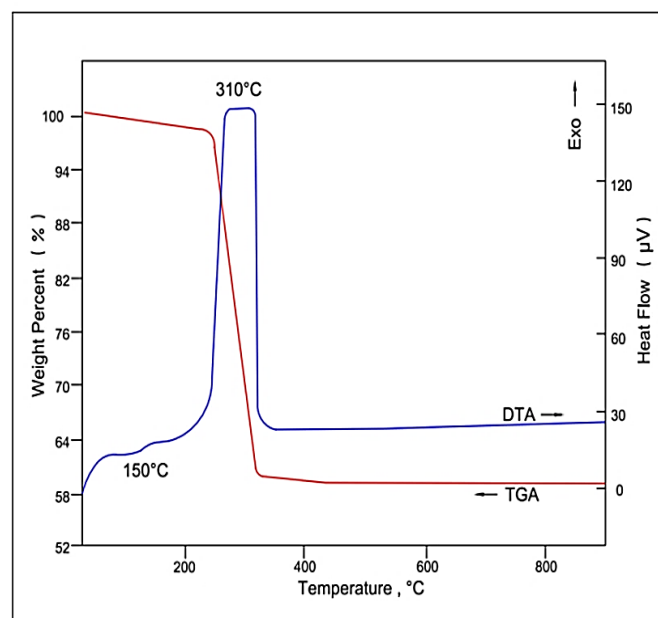
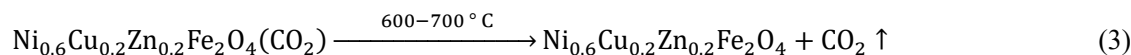
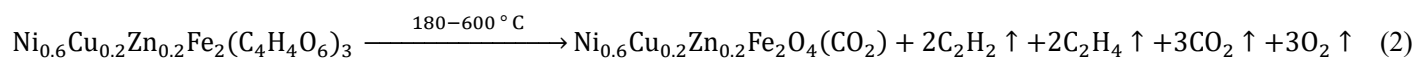
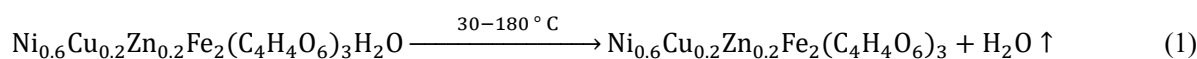


**Fig. 1** TGA and DTA curves for nickel-copper-zinc-iron tartrate monohydrate,  $\text{Ni}_{0.6}\text{Cu}_{0.2}\text{Zn}_{0.2}\text{Fe}_2(\text{C}_4\text{H}_4\text{O}_6)_3 \cdot \text{H}_2\text{O}$ .

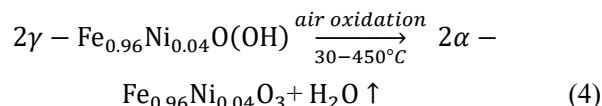
The gaseous product obtained by the thermal decomposition of this precursor was analyzed by qualitative gas detection method. The detailed detection procedure for  $\text{CO}$ ,  $\text{CO}_2$ ,  $\text{C}_2\text{H}_4$ , and  $\text{C}_2\text{H}_2$  was reported elsewhere.<sup>[26]</sup> On the basis of TGA/DTA and complimentary measurement (IR and XRD), the following thermal decomposition pathways of this studied compound may be assumed as follows:

(a) Nickel – copper – zinc – iron tartrate precursor.



A similar thermal decomposition reaction is observed for cobalt–cadmium–iron tartrate, aluminum–cobalt–iron succinate, and cobalt–ruthenium–iron tartrate in a normal air atmosphere.

(b)  $\gamma$ -Ferric–nickel oxyhydroxide



It should be noted here that the  $\gamma$ -phase is obtained at 250 °C and then it is converted to an  $\alpha$ -phase above 450 °C.

### 3.2 Characterization of doped spinel ferrites

#### 3.2.1 Compositional analysis

The composition of doped inverse spinel ferrites such as (a)  $\text{Ni}_{0.6}\text{Cu}_{0.2}\text{Zn}_{0.2}\text{Fe}_2\text{O}_4$ , (b)  $\text{Co}_{0.9}\text{Cd}_{0.1}\text{Fe}_2\text{O}_4$ , (c)  $\text{Al}_{0.3}\text{CoFe}_{1.7}\text{O}_4$ , (d)  $\text{CoRu}_{0.04}\text{Fe}_{1.96}\text{O}_4$ , and (e)  $\text{Fe}_{2.55}\text{Ni}_{0.12}\square_{0.33}\text{O}_4$  was determined by ICPES and EDS analysis. The calculated and observed compositions of elements are summarized in Table 1. The proportion of ingredient elements showed that the weight proportions were correct in the final product.

To see the presence of any impurity element in the sample, we have performed an Energy dispersive X-ray (EDS)

spectroscopy measurement. The EDS studies excluded the presence of any impurity element in all samples. Energy dispersive X-ray analysis. (EDS) spectra (Fig. 2) in all doped ferrites confirmed the presence of the intended substituent’s (dopants) species within the lattice of each crystal examined, and the dopant peak heights relative to those parent elements varied in the correct sense according to the concentration of dopant expected by the nominal composition.

X-ray diffraction pattern (XRD) of all samples such as  $\text{Ni}_{0.6}\text{Cu}_{0.2}\text{Zn}_{0.2}\text{Fe}_2\text{O}_4$ ,  $\text{Co}_{0.9}\text{Cd}_{0.1}\text{Fe}_2\text{O}_4$ ,  $\text{Al}_{0.3}\text{CoFe}_{1.7}\text{O}_4$ ,  $\text{CoRu}_{0.04}\text{Fe}_{1.96}\text{O}_4$  and  $\text{Fe}_{2.55}\text{Ni}_{0.12}\square_{0.33}\text{O}_4$  (*i.e.* nickel doped gamma ferric oxide) are presented in Fig. 3. There is an excellent agreement of observed XRD with the standard JCPDS (File No. 10-325, 21-045, 39-1346) pattern confirming the monophasic spinel structure of these doped ferrites.<sup>[27-30]</sup> The X-ray diffraction peaks are found to be broad, and it is attributed to the nanosized of these spinels. The XRD peaks for these doped spinel ferrites appear approximately at the same position as the respective undoped spinel ferrites but with a slight difference in intensity. The hkl values assigned to the peaks in the XRD are shown in Fig. 3. The observed d-spacing values and relative intensities were compared with

**Table 1.** Observed ICPES and EDS analysis of nanosized doped spinel ferrites.

Compounds	Elemental analysis in wt % ( $\pm 0.5$ )							
	Req	Found	Req	Found	Req	Found	Req	Found
	Fe		Ni		Cu		Zn	
$\text{Ni}_{0.6}\text{Cu}_{0.2}\text{Zn}_{0.2}\text{Fe}_2\text{O}_4$	47.19	47.89 (47.81)*	14.88	15.05 (14.22)	5.37	4.93 (5.16)	5.53	5.85 (5.31)
$\text{NiFe}_2\text{O}_4$	47.65	47.80	25.04	24.91	--	--	--	--
	Fe		Co		Cd		--	--
$\text{Co}_{0.9}\text{Cd}_{0.1}\text{Fe}_2\text{O}_4$	46.54	46.72 (46.33)	22.10	21.91 (22.28)	4.68	4.34 (4.47)	--	--
$\text{CoFe}_2\text{O}_4$	47.60	47.51	25.11	25.01	--	--	--	--
	Fe		Al		Co		--	--
$\text{Al}_{0.3}\text{CoFe}_{1.7}\text{O}_4$	39.49	40.13 (39.37)	3.58	3.71 (3.31)	28.65	28.74 (29.15)	--	--
	Fe		Co		Ru		--	--
$\text{CoRu}_{0.04}\text{Fe}_{1.96}\text{O}_4$	46.29	45.74 (45.95)	24.93	25.04 (24.89)	1.71	1.52 (1.61)	--	--
	Fe		Ni		--	--	--	--
$\text{Fe}_{2.55}\text{Ni}_{0.12}\square_{0.33}\text{O}_4$	66.72	66.80 (66.59)	3.30	3.26 (3.33)	--	--	--	--
$\text{Fe}_{2.67}\square_{0.33}\text{O}_4$	69.97	69.71	--	--	--	--	--	--

\* The figures in parenthesis indicate metal analysis obtained from the EDS method.

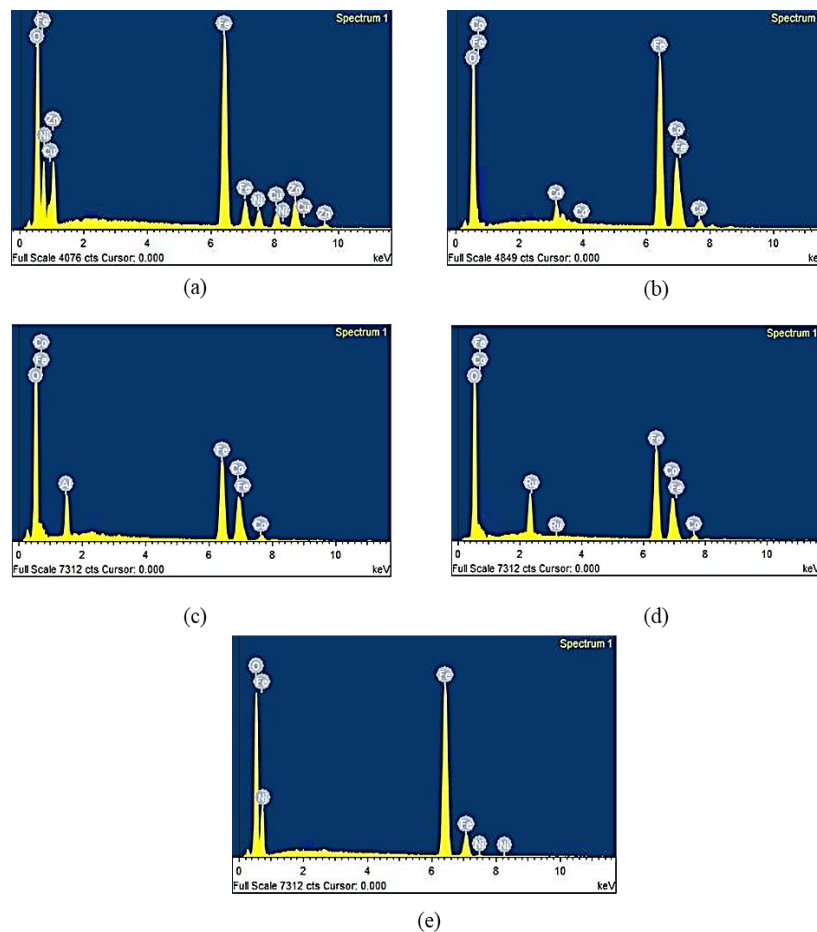


**Fig. 2** Energy dispersive X-ray spectrum (EDS) of nanosized doped spinel ferrites.(a)  $Ni_{0.6}Cu_{0.2}Zn_{0.2}Fe_2O_4$  (b)  $Cd_{0.1}Co_{0.9}Fe_2O_4$  (c) $Al_{0.3}CoFe_{1.7}O_4$  (d)  $CoRu_{0.04}Fe_{1.96}O_4$  (e)  $Fe_{2.55}Ni_{0.12}\square_{0.33}O_4$ .

those reported in the literature.<sup>[27-30]</sup> The lattice parameters have been determined using the relation,  $a = d\sqrt{h^2 + K^2 + l^2}$ , where  $d$  is the inter planer spacing of the diffraction peak and  $h k l$  denotes the Miller indices of the corresponding peaks.

The lattice parameter is given in Table 2. The observed lattice constant of respective undoped spinel ferrites is comparable to the literature.<sup>[11,12,17]</sup> It can also be seen from these tables, the lattice constant increases appreciably with the dopants as compared to respective undoped spinel ferrites (see Table 2). This can be explained based on the relative sizes of ionic radii of different substituent ions, which are relatively larger than that of  $Fe^{3+}$  ions. Replacement of slightly larger dopant cations for smaller  $Fe^{3+}$  cations in the prepared spinel ferrites causes an increase in lattice parameters. There is a correlation between the lattice parameter value and the M – O distance for a particular site in the spinel structure which can directly be correlated to the fraction of every type of  $Co^{2+}$ ,  $Fe^{3+}$ , and substitute cations among these sites.<sup>[31]</sup>

The XRD line width and particle size are connected through the Scherrer equation.<sup>[32]</sup> The crystallite size  $\langle D \rangle_{X\text{-ray}} = 0.9\lambda / \beta \cdot \cos\theta$  with  $\beta^2 = \beta_a^2 - \beta_b^2$ , where  $\langle D \rangle_{X\text{-ray}}$  is the

crystallite diameter,  $\lambda$  is the wavelength of the X-ray radiation,  $\beta$  is the measure of the broadening of diffraction peak due to size effect,  $\beta_a$  and  $\beta_b$  are the full-width at half-maximum of the XRD line of the sample and  $\theta$  is the Bragg’s angle. Using this relation, the observed mean values of the crystallite size  $\langle D \rangle_{X\text{-ray}}$  are depicted in Table 2. As can be seen from Table 2, the mean crystallite size of substituted ferrites is in the range of 18.42 to 34.74 nm indicating the nanosized nature of the samples. The X-ray density of all compounds was determined using the formula  $D_X = 8M / Na^3$ , where ‘M’ is the molecular weight, ‘N’ is Avogadro’s number, and ‘a’ is the lattice parameters. Also, the porosity of the samples was calculated using the relation  $P = (1 - D / D_X)$ , where  $D$  and  $D_X$  are the apparent density and X-ray density, respectively. The results of X-ray density ( $D_X$ ), measured apparent density ( $D$ ), and porosity ( $P$ ) of doped ferrites are given in Table 2. It can be noticed that the X-ray density of each sample is higher than the corresponding apparent density of samples. This may be due to the existence of pores, which were formed and developed during sample preparation. Another reason for the presence of porosity may be the creation of more oxygen

**Table 2.** X-ray diffraction data, particulate properties, and infrared spectral data of nanosized doped spinel ferrites.

Compounds	Lattice constant 'a' nm	Unit cell volume (nm <sup>3</sup> )	Mean crystallite size <D> <sub>x</sub>		X-Ray density D <sub>x</sub> (g.cm <sup>-3</sup> )	Apparent density D (g.cm <sup>-3</sup> )	Porosity P=1-D/D <sub>x</sub>	Average particle size (from histogram) (nm)	Average particle size (from TEM) (nm)	Infrared spectral absorption band cm <sup>-1</sup>	
			Ray	nm ±10%						v <sub>1</sub>	v <sub>2</sub>
Ni <sub>0.6</sub> Cu <sub>0.2</sub> Zn <sub>0.2</sub> Fe <sub>2</sub> O <sub>4</sub>	0.838	0.588	34.74	5.357	5.357	0.75	0.861	47	42	590	405
NiFe <sub>2</sub> O <sub>4</sub>	0.832	--	--	--	--	--	--	--	--	600	410
Co <sub>0.9</sub> Cd <sub>0.1</sub> Fe <sub>2</sub> O <sub>4</sub>	0.840	0.593	33.81	5.498	5.498	0.805	0.854	52	55	601	410
CoFe <sub>2</sub> O <sub>4</sub>	0.835	--	--	--	--	--	--	--	--	606	417
Al <sub>0.3</sub> CoFe <sub>1.7</sub> O <sub>4</sub>	0.837	0.586	27.53	5.192	5.192	0.649	0.988	37	34	611	418
CoRu <sub>0.04</sub> Fe <sub>1.96</sub> O <sub>4</sub>	0.839	0.591	30.87	5.297	5.297	0.796	0.850	33	29	611	414
										435	
Fe <sub>2.55</sub> Ni <sub>0.12</sub> □ <sub>0.33</sub> O <sub>4</sub>	0.837	0.586	18.42	4.874	4.874	0.926	0.810	18	20	543	(shoulder at 472)
Fe <sub>2.67</sub> □ <sub>0.33</sub> O <sub>4</sub>	0.834	--	--	--	--	--	--	--	--	550	443

vacancies (as required by the charge balance) in the doped samples as compared to undoped samples, and as a result, fewer cations are created in the system.<sup>[33]</sup>

Microstructure plays an important role in obtaining the desired electric and magnetic particles of these materials for their microwave absorption applications. The microstructure and morphology of Ni<sub>0.6</sub>Cu<sub>0.2</sub>Zn<sub>0.2</sub>Fe<sub>2</sub>O<sub>4</sub>, Co<sub>0.9</sub>Cd<sub>0.1</sub>Fe<sub>2</sub>O<sub>4</sub>, Al<sub>0.3</sub>CoFe<sub>1.7</sub>O<sub>4</sub>, CoRu<sub>0.04</sub>Fe<sub>1.96</sub>O<sub>4</sub>, and Fe<sub>2.55</sub>Ni<sub>0.12</sub>□<sub>0.33</sub>O<sub>4</sub>

samples were observed by scanning electron microscopy (SEM), as shown in Fig. 4. As it can be seen from the figure (a-d), the obtained nanoparticles get interlocked with each other to form a cluster. However, close observation shows the agglomerates of nearly spherical particles. The SEM image of the Fe<sub>2.55</sub>Ni<sub>0.12</sub>□<sub>0.33</sub>O<sub>4</sub> sample indicates that the morphology is characterized by an acicular shape of particles and agglomerated due to the magnetic interaction (see Fig. 4 (e)).

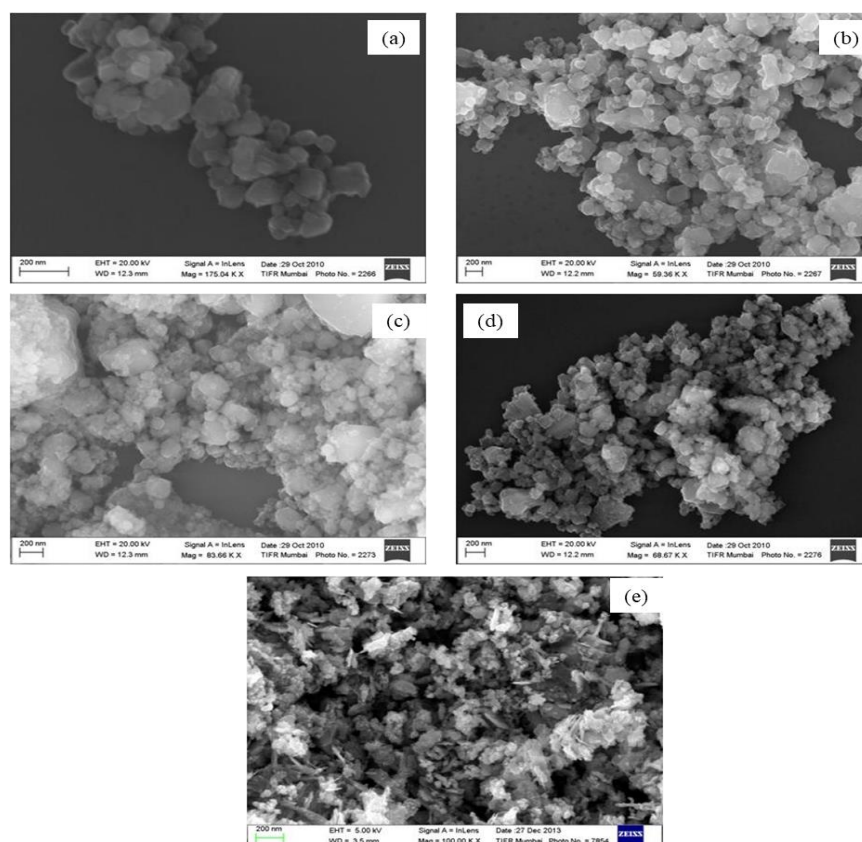


**Fig. 4** Scanning electron micrographs (SEM) of nanosized doped spinel ferrites. (a) Ni<sub>0.6</sub>Cu<sub>0.2</sub>Zn<sub>0.2</sub>Fe<sub>2</sub>O<sub>4</sub>, (b) Cd<sub>0.1</sub>Co<sub>0.9</sub>Fe<sub>2</sub>O<sub>4</sub>, (c) Al<sub>0.3</sub>CoFe<sub>1.7</sub>O<sub>4</sub>, (d) CoRu<sub>0.04</sub>Fe<sub>1.96</sub>O<sub>4</sub>, (e) Fe<sub>2.55</sub>Ni<sub>0.12</sub>□<sub>0.33</sub>O<sub>4</sub>.

Domain wall exists when grain size in the obtained spinel ferrites and grain size of these ferrites powder in the matrix become larger (*i.e.*, samples were coated by a gold thin film by using a sputtering technique, before observation in SEM) than critical grain size ( $D_c$ ) is given by the following expression.<sup>[34]</sup>

$$D_c = 18 \mu_0 \sigma_w / M_s^2 \quad (5)$$

where  $\sigma_w$  is the domain wall and  $M_s$  is the saturation magnetization of the sample. So, the magnetic loss ( $\mu_0$ ) due to displacement of the domain wall is added to magnetic losses.

The histogram of the particle size was drawn and has been shown in Fig. 5. The average size of all doped spinel ferrite ranges between 18nm and 52nm as per histogram obtained from SEM (see Table 2). The morphology of the particles formed was examined by transmission electron microscopy (TEM) for these doped spinel ferrites. The micrographs (TEM) and SAED patterns of all samples are given in Fig. 6. The variation of particle size is predominantly seen for these ferrites. TEM images of these doped spinel ferrites (Fig. 6(a)

(e)) show the grains to be in the nanometer size range, indicating the nanocrystalline nature of the compounds. The average grain sizes, measured by taking around 10 - 15 grains during the measurement stage, are found to be 20 to 55 nm range. The average particle sizes of these powders are given in Table 2. The grain shape of all samples is roughly spherical and not highly agglomerated (see Fig. 6(a)' to (e)'). The structural information from the selected area electron diffraction (SAED) pattern Fig. 6(a) - (e) shows the crystalline nature. It is apparent that all these lattice planes are clearly distinct in the SAED pattern (see Fig. 6(a)' to (e)'). The reflections correspond to (311), (511), and (440) lattice planes, which are also signatures of an FCC spinel phase. These values were indexed to the single-phase cubic structure of the doped inverse spinel ferrites. In addition, it may be noted that the High-Resolution Transmission Electron Microscopy (HRTEM) of semiconductor oxide reported in the literature<sup>[35]</sup> could indicate the presence of lattice distinct fringes and confirming the nanocrystalline nature and good crystallinity.

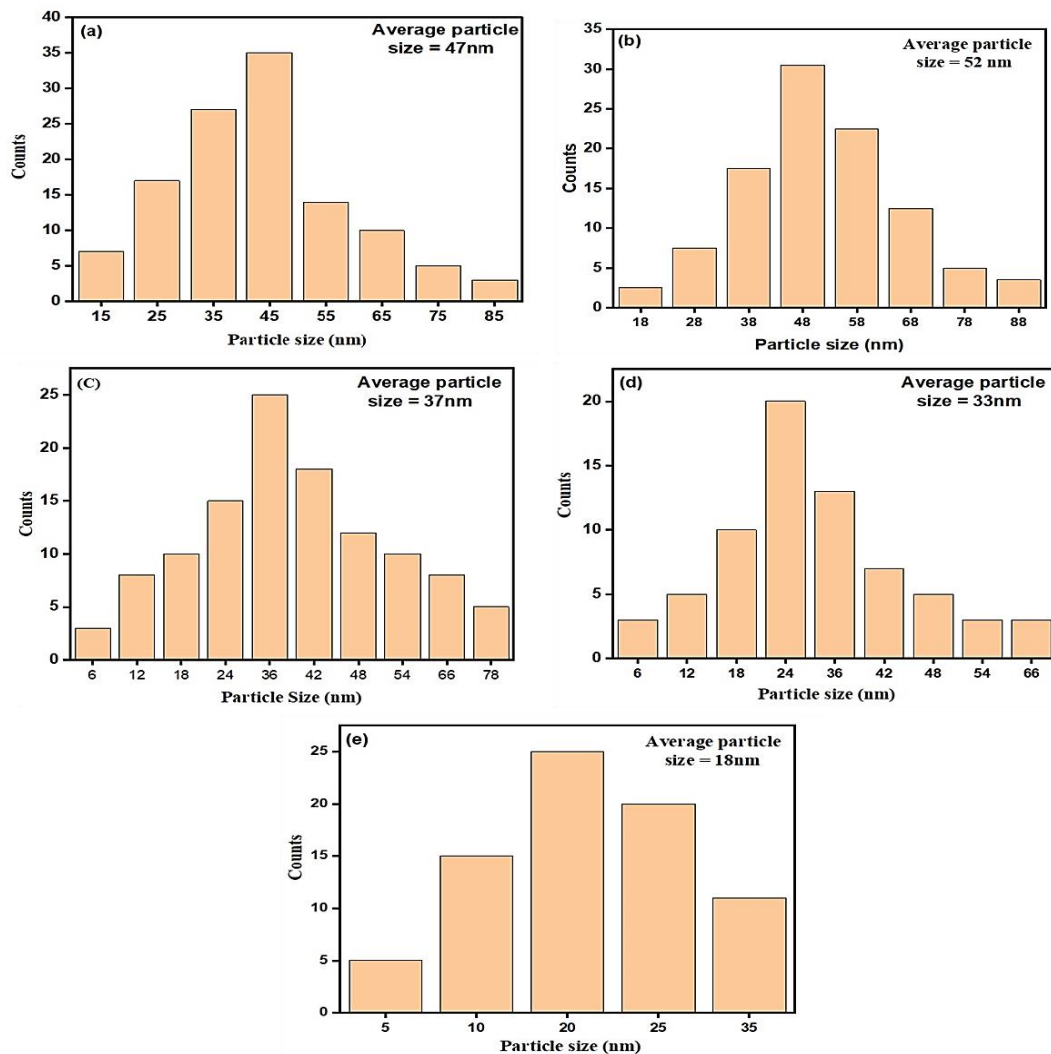
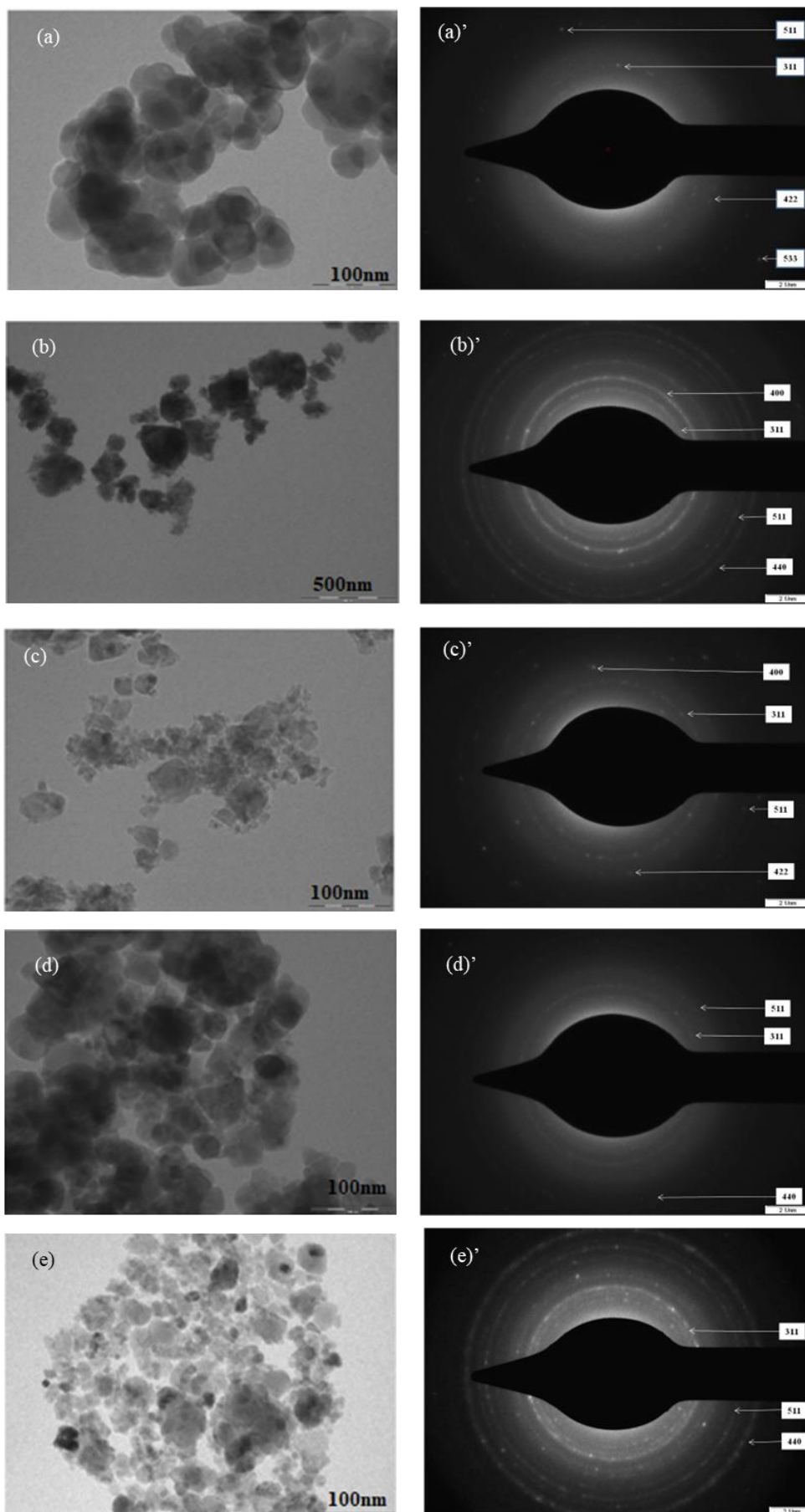


Fig. 5 Histogram of the particle size distribution for doped spinel ferrites. (a) Ni<sub>0.6</sub>Cu<sub>0.2</sub>Zn<sub>0.2</sub>Fe<sub>2</sub>O<sub>4</sub>, (b) Co<sub>0.9</sub>Cd<sub>0.1</sub>Fe<sub>2</sub>O<sub>4</sub>, (c) Al<sub>0.3</sub>CoFe<sub>1.7</sub>O<sub>4</sub>, (d) CoRu<sub>0.04</sub>Fe<sub>1.96</sub>O<sub>4</sub> (e) Fe<sub>2.55</sub>Ni<sub>0.12</sub>□<sub>0.33</sub>O<sub>4</sub>.



**Fig. 6** Transmission electron micrographs (TEM) and Selected area electron diffraction (SAED) pattern of nanosized doped spinel ferrites. (a)  $Ni_{0.6}Cu_{0.2}Zn_{0.2}Fe_2O_4$ , (b)  $Cd_{0.1}Co_{0.9}Fe_2O_4$ , (c)  $Al_{0.3}CoFe_{1.7}O_4$ , (d)  $CoRu_{0.04}Fe_{1.96}O_4$ , (e)  $Fe_{2.55}Ni_{0.12}\square_{0.33}O_4$ .

The infrared spectra of investigated doped ferrites viz.  $\text{Ni}_{0.6}\text{Cu}_{0.2}\text{Zn}_{0.2}\text{Fe}_2\text{O}_4$ ,  $\text{Co}_{0.9}\text{Cd}_{0.1}\text{Fe}_2\text{O}_4$ ,  $\text{Al}_{0.3}\text{CoFe}_{1.7}\text{O}_4$ ,  $\text{CoRu}_{0.04}\text{Fe}_{1.96}\text{O}_4$  and  $\gamma\text{-Fe}_{2.55}\text{Ni}_{0.12}\square_{0.33}\text{O}_4$  showed somewhat broad bands  $\nu_1$  at  $\sim 590\text{ cm}^{-1}$  and  $\nu_2$  at  $405\text{ cm}^{-1}$  (see Fig. 7). The  $\nu_1$  and  $\nu_2$  bands are assigned to intrinsic vibrations of tetrahedral and octahedral groups respectively.<sup>[36]</sup> The infrared bands for all samples under investigation are given in Table 2. It can be seen that the frequencies  $\nu_1$  and  $\nu_2$  are shifted slightly to the lower frequency side on doping as compared to respective undoped spinel ferrite. A very small change is observed in the absorption band for doped samples, which may be due to the differences in the microstructures. The observed band position for all doped ferrites is at high-frequency band  $\nu_1$  ranging from  $543$  to  $611\text{ cm}^{-1}$ , and the lower  $\nu_2$  band is in the range from  $405$  to  $435\text{ cm}^{-1}$ . This difference is expected because of the difference in the  $\text{Fe}^{3+} - \text{O}^{2-}$  distances for octahedral and tetrahedral complexes. The splitting in  $\nu_2$  is evidence of a contribution of  $\text{Fe}^{2+}$  on the octahedral sites, and the ferrite becomes normal  $\nu_1$  and  $\nu_2$  depending on the nature of the octahedral cations and less on the tetrahedral ions.

Thus, splitting of  $\nu_1$  and  $\nu_2$  into the shoulder has not been observed in the present doped compounds, except  $\gamma\text{Fe}_{2.55}\text{Ni}_{0.12}\square_{0.33}\text{O}_4$  compound, which also confirms the absence of excessive  $\text{Fe}^{2+}$  ions. While  $\gamma\text{Fe}_{2.55}\text{Ni}_{0.12}\square_{0.33}\text{O}_4$  (*i.e.*, nickel doped gamma ferric oxide) compound showed splitting of  $\nu_2$  into the shoulder (at  $472\text{ cm}^{-1}$ ), which shows the presence of  $\text{Fe}^{2+}$  ions at the octahedral site (see Fig. 7).

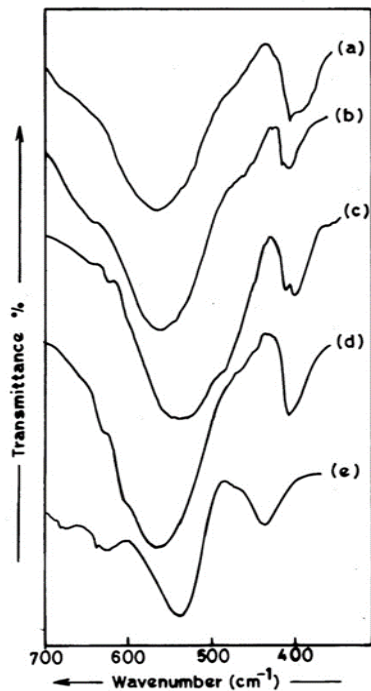


**Fig. 7** Infrared spectra of nanosized doped spinel ferrites. (a)  $\text{Ni}_{0.6}\text{Cu}_{0.2}\text{Zn}_{0.2}\text{Fe}_2\text{O}_4$ , (b)  $\text{Co}_{0.9}\text{Cd}_{0.1}\text{Fe}_2\text{O}_4$ , (c)  $\text{Al}_{0.3}\text{CoFe}_{1.7}\text{O}_4$ , (d)  $\text{CoRu}_{0.04}\text{Fe}_{1.96}\text{O}_4$  (e)  $\text{Fe}_{2.55}\text{Ni}_{0.12}\square_{0.33}\text{O}_4$ .

### 3.2.3 Electrical conductivity studies

The temperature dependence of electrical conductivity,  $\sigma$ , of  $\text{Ni}_{0.6}\text{Cu}_{0.2}\text{Zn}_{0.2}\text{Fe}_2\text{O}_4$ ,  $\text{Co}_{0.9}\text{Cd}_{0.1}\text{Fe}_2\text{O}_4$ ,  $\text{Al}_{0.3}\text{CoFe}_{1.7}\text{O}_4$ ,  $\text{CoRu}_{0.04}\text{Fe}_{1.96}\text{O}_4$ , and  $\text{Fe}_{2.55}\text{Ni}_{0.12}\square_{0.33}\text{O}_4$  compounds is presented in Fig. 8. The experiments are repeated three times, and the results are always found to be reproducible. The plot of  $\log \sigma$  against  $T^{-1}$  obeys the Arrhenius relation  $\sigma = \sigma_0 \exp(-E_a/KT)$ , suggesting the semiconducting nature of all doped spinel ferrites, where  $E_a$  is the activation energy,  $\sigma_0$  is temperature-independent constant,  $K$  is Boltzmann constant, and  $T$  is the absolute temperature. The electrical conductivity ( $\log \sigma$ ) was plotted versus the reciprocal of absolute temperature ( $T^{-1}$ ). The slope of these lines was considered to give the activation energy  $E_a$  for the semiconduction of these doped spinel ferrite compounds. The plot of  $\log \sigma$  versus  $T^{-1}$  for these doped inverse spinel ferrites (Fig. 8) shows an initial decrease in electric conductivity in the temperature range of  $35$  to  $130\text{ }^\circ\text{C}$ . The  $\sigma$  values are then increased, showing two distinct slopes with a ‘break’. The initial decrease in conductivity in the temperature range  $345\text{ K}$  to  $400\text{ K}$  corresponds to the desorption of adsorbed water molecules, usually adsorbed water molecules behave as electron donors. These figures also show that there are two temperature regions with different activation energies. The temperature at which the break occurs was found to be about  $525\text{ K}$  *i.e.*, transition temperature  $T_c$  (see Table 3). The break will be most marked for all compounds in which there is a strong exchange interaction between the outer and inner electrons. In addition, a different dopant can be affected by many factors like the nature of the dopant, the number of dopants incorporated, creating structural defects, and changing its microstructures. Therefore, we turn to the magnetic behavior of these compounds. The conductivity does not exhibit much variation with the temperature at region A due to the hopping of defect-related weakly bonded electrons are responsible for conduction, while conduction at high-temperature region B (above  $T_c$ ) corresponds to the hopping of thermally activated charge carriers in these doped spinel ferrites.

The activation energies ( $E_a$ ) are calculated for the two regions around breakpoints, firstly for ferrimagnetic (region A) and secondly for the paramagnetic region (region B) applying the above relates to the plot of  $\log \sigma$  versus  $T^{-1}$  (Fig. 8), and the results are listed in Table 3. From this table, the values of activation energies ( $E_a$ ) for doped ferrites are appreciably less than the respective undoped spinel ferrite. The activation energy ( $E_a$ ) in the paramagnetic region is higher than that in the ferrimagnetic region. The observed  $E_a$  can be attributed to dopant ions in the present study such as  $\text{Ni}^{2+}$ ,  $\text{Cu}^{2+}$ ,  $\text{Co}^{2+}$ ,  $\text{Al}^{3+}$ ,  $\text{Ru}^{3+}$ , *etc.* ions that are known to have a strong preference for

**Table 3.** Electrical conductivity data and Hall effect of nanosized doped spinel ferrites.

Compounds	Temperature corresponding to desorption of adsorbed H <sub>2</sub> O molecule T (K)	Conductivity measurements			Hall effect measurements					
		Region	Temp. range (K)	Activation energy Ea (ev)	Break temp. (transition temperature) T <sub>c</sub> (K)	Current passed (nA)	Resistivity at room temp. Ohm cm	Types of charge carriers	Average Hall coefficient cm <sup>3</sup> /C	Mobility cm <sup>2</sup> /Vs
Ni <sub>0.6</sub> Cu <sub>0.2</sub> Zn <sub>0.2</sub> Fe <sub>2</sub> O <sub>4</sub>	384	A	303-525	0.744	525	-	-	n-Type	-	-
		B	525-805	0.836						
NiFe <sub>2</sub> O <sub>4</sub>	405	A	300-505	0.801	536	-	-	n-Type	-	-
		B	520-500	0.893						
Co <sub>0.9</sub> Cd <sub>0.1</sub> Fe <sub>2</sub> O <sub>4</sub>	345	A	303-475	0.603	475	20	4.727 x 10 <sup>7</sup>	n-Type	-1.290 x 10 <sup>10</sup>	273.0
		B	475-825	0.912						
CoFe <sub>2</sub> O <sub>4</sub>	340	A	305-481	0.713	500	-	-	n-Type	-	-
		B	450-830	0.978						
Al <sub>0.3</sub> CoFe <sub>1.7</sub> O <sub>4</sub>	400	A	303-558	0.694	558	20	2.085 x 10 <sup>8</sup>	n-Type	-6.342x 10 <sup>9</sup>	30.81
		B	558-750	0.970						
CoRu <sub>0.04</sub> Fe <sub>1.96</sub> O <sub>4</sub>	375	A	303-525	0.455	525	20	2.155 x 10 <sup>7</sup>	n-Type	-9.571x 10 <sup>9</sup>	444.1
		B	525-805	0.772						
Fe <sub>2.55</sub> Ni <sub>0.12</sub> □ <sub>0.33</sub> O <sub>4</sub>	399	A	303-553	0.692	553	10	5.047 x 10 <sup>7</sup>	n-Type	-3.399x 10 <sup>9</sup>	67.35
		B	553-805	1.313						
Fe <sub>2.67</sub> □ <sub>0.33</sub> O <sub>4</sub>	380	A	300-545	0.850	--	--	--	n-Type	--	--
		B (α-phase)	550-800	1.350						

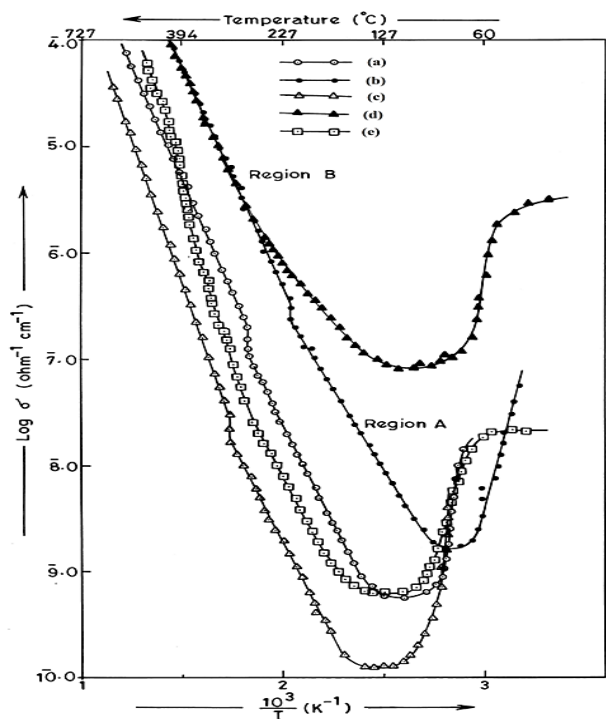


**Fig. 8** Plot of log  $\sigma$  against  $T^{-1}$  of nanosized doped spinel ferrites. (a) Ni<sub>0.6</sub>Cu<sub>0.2</sub>Zn<sub>0.2</sub>Fe<sub>2</sub>O<sub>4</sub>, (b) Co<sub>0.9</sub>Cd<sub>0.1</sub>Fe<sub>2</sub>O<sub>4</sub>, (c) Al<sub>0.3</sub>CoFe<sub>1.7</sub>O<sub>4</sub>, (d) CoRu<sub>0.04</sub>Fe<sub>1.96</sub>O<sub>4</sub> (e) Fe<sub>2.55</sub>Ni<sub>0.12</sub>□<sub>0.33</sub>O<sub>4</sub>.

octahedral B-site, while Zn<sup>2+</sup> and Cd<sup>2+</sup> occupy at tetrahedral A-site. They are all depending on the crystal field stabilization energies of the metal ion.<sup>[37]</sup> These dopants may be occupied at

interstitial or vacancy (i.e., point defect) of spinel lattices. Therefore, the conductivity of impurity (dopant) is a favour in the ferrimagnetic region, while the electron hopping in the sublattice between Fe<sup>2+</sup> → Fe<sup>3+</sup> ion results in increased activation energy (Ea) in the paramagnetic region. Magensen *et al.*<sup>[38]</sup> as shown that dopants with lower valences may also lead to the introduction of vacancies, whereas dopants with higher valences may remove the oxygen vacancies. Apart from the charge state, these dopant ions do not participate in conduction processes but limit the degree of Fe<sup>2+</sup> - Fe<sup>3+</sup> condition, which is described by the Verway-deBoer mechanism.<sup>[39]</sup> According to this phenomenon, the excess electrons on oxygen then bond with the neighboring Fe<sup>3+</sup> ions in the spinel lattice due to electrostatic interaction giving rise to Fe<sup>2+</sup> ions. The overall charge balance is restored by oxygen loss from the sample. The formation of Fe<sup>2+</sup> ion leads to the deviation from the spinel ferrite stoichiometry.

The Seebeck voltage against temperature measurements for all doped spinel ferrites (Fig. 9) shows an initial fall in the negative charge carrier in the temperature range 325 to 450 K, and the number remains almost constant upto 580 K and then negative Seebeck voltage increases with increasing temperature. While Fe<sub>2.55</sub>Ni<sub>0.12</sub>□<sub>0.33</sub>O<sub>4</sub> sample, the negative Seebeck voltage above 580 K becomes positive and its magnitude increases with increasing temperature upto 750K.

The Seebeck voltage for Ni<sub>0.6</sub>Cu<sub>0.2</sub>Zn<sub>0.2</sub>Fe<sub>2</sub>O<sub>4</sub>, Co<sub>0.9</sub>Cd<sub>0.1</sub>Fe<sub>2</sub>O<sub>4</sub>, Al<sub>0.3</sub>CoFe<sub>1.7</sub>O<sub>4</sub>, and CoRu<sub>0.04</sub>Fe<sub>1.96</sub>O<sub>4</sub> and

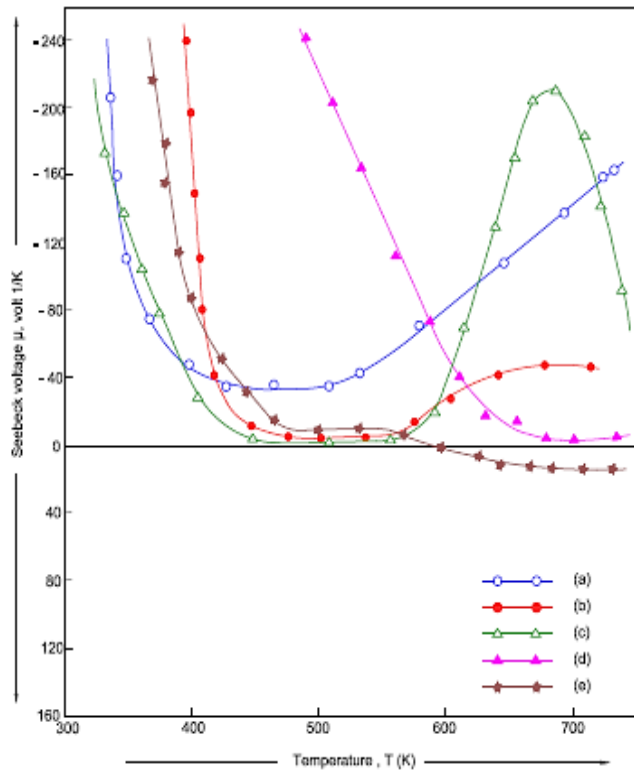


**Fig. 9** Plot of Seebeck voltage,  $\mu$  (volt  $K^{-1}$ ) against temperature,  $T$  (K) for nanosized doped spinel ferrites. (a)  $Ni_{0.6}Cu_{0.2}Zn_{0.2}Fe_2O_4$ , (b)  $Co_{0.9}Cd_{0.1}Fe_2O_4$ , (c)  $Al_{0.3}CoFe_{1.7}O_4$ , (d)  $CoRu_{0.04}Fe_{1.96}O_4$  (e)  $Fe_{2.55}Ni_{0.12}\square_{0.33}O_4$ .

$Fe_{2.55}Ni_{0.12}\square_{0.33}O_4$  samples are n-type semiconductivity. Verwey and deBoer<sup>[39]</sup> have established that in oxide spinels containing one ion of variable valence, the conduction takes place by hopping via activation of state involving cation change valence as  $Fe^{2+} \leftrightarrow Fe^{3+}$  and vice versa, which leads to electronic conduction of negative charge carrier for samples except for  $Fe_{2.55}Ni_{0.12}\square_{0.33}O_4$  sample. In contrast for  $Fe_{2.55}Ni_{0.12}\square_{0.33}O_4$  sample above 580 K, showed a hole-mediated conduction mechanism that seems to be dominant *i.e.* p-type semiconductivity. (the presence of an excess of oxygen in this sample provides  $Ni^{3+}$  sites which allow motion of holes between  $Ni^{2+}$  to  $Ni^{3+}$  ions by a thermally activated process in the system). So the low Seebeck values for  $Fe_{2.55}Ni_{0.12}\square_{0.33}O_4$  sample may be due to electron-hole compensation.

These studies, also measured the Hall effect constantly in the magnetic field of 0.54 T at room temperature after passing current in nano Ampere. These results are listed in Table 3 for all doped samples except  $Ni_{0.6}Cu_{0.2}Zn_{0.2}Fe_2O_4$ , which do not show Hall constant values because of high resistivity. The high resistivity was found due to the small value of charge mobility and the increase in B – the site hopping length of this sample. The specific resistivity values were observed for all doped inverse spinel ferrites around  $2.155 \times 10^7$  to  $2.055 \times 10^8$  ohm-

cm at current passed from 10 to 20 nA. The variation in the observed specific resistivities is also reflected in mobility. The Hall coefficient at room temperature for all compounds is negative, indicating the electrons are the majority carriers. The observed Hall coefficient variations are also corresponding to mobility. This may suggest that the specific resistivity and Hall coefficient are mainly governed by the charge carrier mobility rather than a carrier.

### 3.2.4 Dielectric studies

The dielectric constant ( $\epsilon'$ ) and dielectric loss ( $\tan \delta$ ) against the log of frequency in the range 1-600 kHz were recorded at room temperature for doped spinel ferrites such as (a)  $Ni_{0.6}Cu_{0.2}Zn_{0.2}Fe_2O_4$ , (b)  $Co_{0.9}Cd_{0.1}Fe_2O_4$ , (c)  $Al_{0.3}CoFe_{1.7}O_4$ , (d)  $CoRu_{0.04}Fe_{1.96}O_4$  (e)  $Fe_{2.55}Ni_{0.12}\square_{0.33}O_4$  compounds. The representative of dielectric constant ( $\epsilon'$ ) versus the log of frequencies of  $Ni_{0.6}Cu_{0.2}Zn_{0.2}Fe_2O_4$  is shown in Fig. 10 (a). Similar nature of dielectric loss ( $\tan \delta$ ) against the log of frequency is also observed for this doped spinel ferrite (see Fig. 10 (b)). The value of dielectric constant ( $\epsilon'$ ) decreases with increasing frequency upto 110 kHz and then remains constant (see Fig. 10 (a)). The decrease of the dielectric constant ( $\epsilon'$ ) with dopant ions can be explained based on the mechanism of the polarization process in ferrites. The whole polarization in ferrites is mainly contributed by the space charge polarization and hopping exchange of the charges between two localized states governed by the density of the localized state and the resultant displacement of charges with respect to the external field. The addition of substituents (dopants) reduces the iron ions on B – site, which is responsible for both space charge polarization and hopping exchange between the localized states. The decrease in dielectric constant ( $\epsilon'$ ) with increasing frequency is attributed to the fact that the electron exchange between  $Fe^{2+}$  and  $Fe^{3+}$  ions cannot follow the change of the externally applied field beyond a certain frequency, *i.e.*, weak polarization.<sup>[40]</sup> The value of the dielectric constant ( $\epsilon'$ ) is very high at lower frequencies and decreases with increasing frequency up to 110 kHz and then remains constant up to  $10 \times 10^3$  kHz. At this stage, domain wall motion occurs.

The values of dielectric loss ( $\tan \delta$ ) decrease monotonically with an increase in log frequency for this sample. Generally, the dielectric loss in ferrites is considered to originate from two mechanisms: electron hopping and charged defect dipoles. The former contributes to dielectric loss in the low-frequency range, is due to electron hopping, while in the high-frequency range, dielectric loss main results from the response of the defect dipoles to the field. These dipoles in ferrites are formed due to changes in the cation state, such as  $Fe^{+3}/Fe^{2+}$ , during the sintering process. Relaxation of dipoles under an electric field

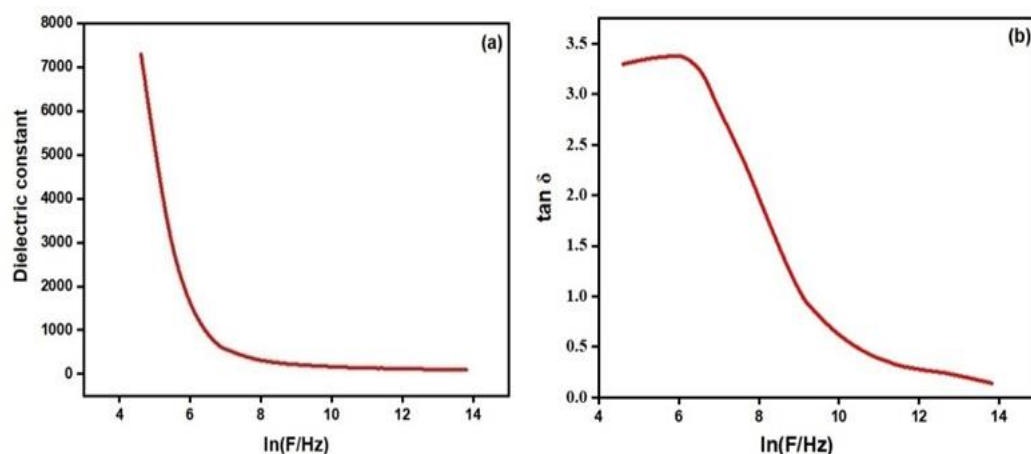


**Fig. 10** (a) Plot of variation of dielectric constant ( $\epsilon'$ ) and (b) dielectric loss ( $\tan \delta$ ) with frequency for  $\text{Ni}_{0.6}\text{Cu}_{0.2}\text{Zn}_{0.2}\text{Fe}_2\text{O}_4$ .

is decreased with increasing frequency and ultimately results in a decrease in the dielectric loss in the high-frequency range.

### 3.2.5 Magnetic studies

Magnetization measurement of  $\text{Ni}_{0.6}\text{Cu}_{0.2}\text{Zn}_{0.2}\text{Fe}_2\text{O}_4$ ,  $\text{Co}_{0.9}\text{Cd}_{0.1}\text{Fe}_2\text{O}_4$ ,  $\text{Al}_{0.3}\text{CoFe}_{1.7}\text{O}_4$ ,  $\text{CoRu}_{0.04}\text{Fe}_{1.96}\text{O}_4$ , and  $\text{Fe}_{2.55}\text{Ni}_{0.12}\square_{0.33}\text{O}_4$  and respective undoped spinel ferrites (i.e.  $\text{NiFe}_2\text{O}_4$ ,  $\text{CoFe}_2\text{O}_4$  and  $\gamma\text{-Fe}_{2.67}\square_{0.33}\text{O}_4$ ) samples were carried out using a vibrating sample magnetometer (VSM) with the maximum applied field of 8 KOe at room temperature. The obtained hysteresis loops are shown in Fig. S3 of the supplementary information file and were found to be saturated with the available applied field. The representative hysteresis loop (i.e. magnetization versus applied field) for  $\text{Fe}_{2.55}\text{Ni}_{0.12}\square_{0.33}\text{O}_4$  is shown here in Fig. 11. From the hysteresis loops, the magnetic parameters such as coercive force ( $H_c$ ), saturation magnetization ( $M_s$ ), a ratio of remanence to saturation magnetization ( $M_R/M_s$ ) and magnetic moment ( $n_B$ ) values have been calculated and are listed in Table 4. It can be seen that the observed magnetic parameters for respective undoped spinel ferrites are very close to the reported in the literature.<sup>[11,12,17]</sup> However these magnetic parameters of undoped samples (such as  $\text{NiFe}_2\text{O}_4$ ,  $\text{CoFe}_2\text{O}_4$ , and  $\text{Fe}_{2.67}\square_{0.33}\text{O}_4$ ) are consistent with reports of S. Chakrabarti *et al.*<sup>[20]</sup> They observed a decrease in the values of magnetic parameters of  $\text{NiFe}_2\text{O}_4$  ( $M_s = 61.3\text{ emu/g}$ ,  $H_c = 53.0\text{ Oe}$ ),  $\text{CoFe}_2\text{O}_4$  ( $M_s = 63\text{ emu/g}$ ,  $H_c = 2205\text{ Oe}$ ), and  $\text{Fe}_{2.67}\square_{0.33}\text{O}_4$  ( $M_s = 60\text{ emu/g}$ ,  $H_c = 352\text{ Oe}$ ) are prepared by salt-assisted and Citrate gel autocombustion method, respectively, which depends on size, shape as well as a preparation method. In addition, the smaller grain size leads to a reduction in magnetic parameters for these samples.

The increase in observed coercivity ( $H_c$ ) for all doped samples except  $\text{Fe}_{2.55}\text{Ni}_{0.12}\square_{0.33}\text{O}_4$  sample as compared to respective undoped ferrites are indicative of

magnetocrystalline anisotropy (see Table 4). Coercivity is a structural-related extrinsic element. It is also known that when porosity is high, the average particle size would be smaller, and the value of coercivity ( $H_c$ ) would be high. From Table 4, it is cleared that porosity increases due to which coercivity enhances.<sup>[41]</sup> Another reason is that the defect formation in these spinel ferrites (in the form of point defects) also results in higher coercivity.<sup>[42]</sup> According to Li *et al.*<sup>[43]</sup>, the longitudinal magnetic recording medium, which is the general type of magnetic recording medium used in industries, requires high enough coercivity (around 800 Oe). If coercivity is too high (above 1200 Oe), the material can be used for the perpendicular recording media, which is a developing new technology in magnetic recording media.<sup>[43]</sup> In the present investigation, the coercivity is in the range of 72.87 - 811 Oe for all doped samples except  $\text{CoRu}_{0.04}\text{Fe}_{1.96}\text{O}_4$  sample, so the material can be applied to longitudinal magnetic recording media. While the coercivity of  $\text{CoRu}_{0.04}\text{Fe}_{1.96}\text{O}_4$  sample has 1218 Oe and therefore this material can be applied in the perpendicular magnetic recording media.<sup>[43]</sup>

It can also be observed from Table 4 the saturation magnetization ( $M_s$ ), and Remanence ratio ( $M_R/M_s$ ) decrease for all doped ferrites as compared to the respective undoped spinel ferrite. The  $M_R/M_s$  ratio (i.e. squareness) below 0.5 signifies that the material has a multi-domain structure, while more than 0.5 indicate that the material has a single-domain structure.<sup>[44]</sup> In the present investigation, the ratio of  $M_R/M_s$  is found between 0.11 to 0.47 indicating prepared samples such as  $\text{Ni}_{0.6}\text{Cu}_{0.2}\text{Zn}_{0.2}\text{Fe}_2\text{O}_4$ ,  $\text{Co}_{0.9}\text{Cd}_{0.1}\text{Fe}_2\text{O}_4$ ,  $\text{Al}_{0.3}\text{CoFe}_{1.7}\text{O}_4$ , and  $\text{CoRu}_{0.04}\text{Fe}_{1.96}\text{O}_4$  possesses a multi-domain structure, while  $\text{Fe}_{2.55}\text{Ni}_{0.12}\square_{0.33}\text{O}_4$  sample possesses  $M_R/M_s$  ratio 0.58, suggesting a single domain magnetic structure the values of squareness ratio  $M_R/M_s$  for undoped ferrites such as  $\text{NiFe}_2\text{O}_4$ ,  $\text{CoFe}_2\text{O}_4$ , and  $\gamma\text{-Fe}_{2.67}\square_{0.33}\text{O}_4$  are 0.55 0.65 and 0.68, respectively, which also confirms the single-domain structure.

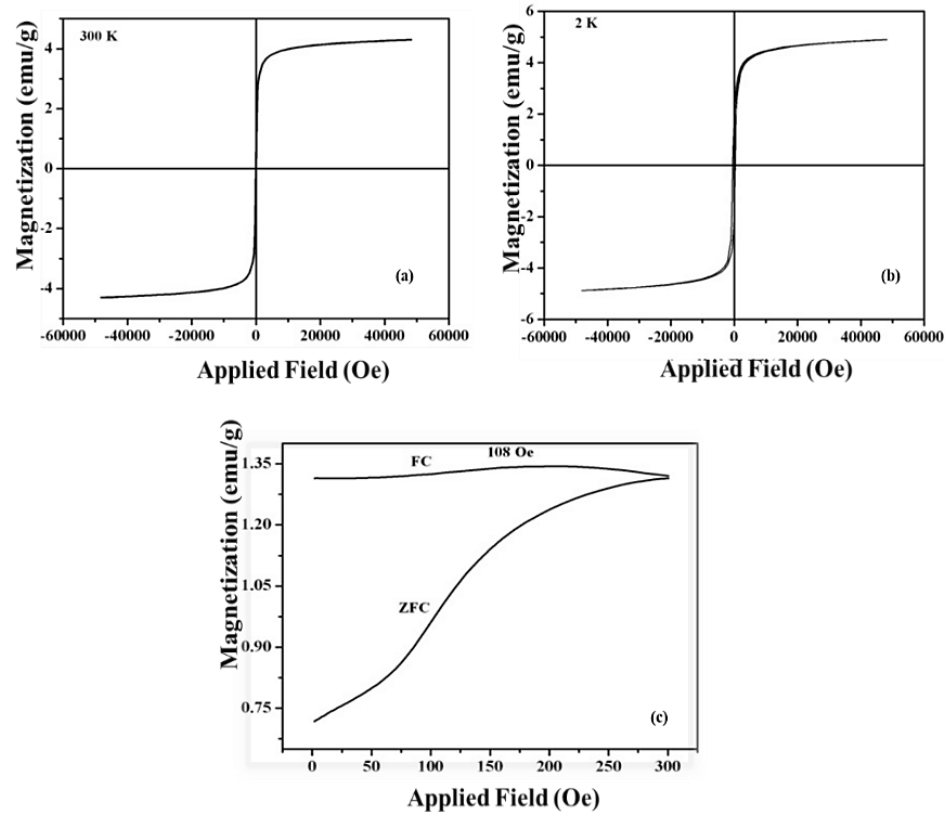


**Fig. 11** Magnetization Vs Applied field and ZFC and FC magnetization against the temperature of nickel-doped gamma ferric oxide  $Fe_{2.55}Ni_{0.12}□_{0.33}O_4$ .

**Table 4.** Magnetic properties for nanosized doped spinel ferrites.

Compounds	Coercive force Hc ± 0.5 Oe	The saturation magnetization (Ms) ±2 emu / g	Ratio of M <sub>R</sub> / M <sub>s</sub>	Magnetic moment n <sub>B</sub> ±0.1 μ <sub>B</sub>	
				Observed	Calculated
Ni <sub>0.6</sub> Cu <sub>0.2</sub> Zn <sub>0.2</sub> Fe <sub>2</sub> O <sub>4</sub>	72.87	42.34	0.11	1.80	5.31
NiFe <sub>2</sub> O <sub>4</sub>	72.01	63.00	0.55	2.21	2.83
Co <sub>0.9</sub> Cd <sub>0.1</sub> Fe <sub>2</sub> O <sub>4</sub>	811.01	65.16	0.35	2.86	5.46
CoFe <sub>2</sub> O <sub>4</sub>	680	91.8	0.65	3.85	3.87
Al <sub>0.3</sub> CoFe <sub>1.7</sub> O <sub>4</sub>	789.54	32.76	0.47	1.34	2.64
CoRu <sub>0.04</sub> Fe <sub>1.96</sub> O <sub>4</sub>	1218.1	54.78	0.47	2.31	3.87
Fe <sub>2.55</sub> Ni <sub>0.12</sub> □ <sub>0.33</sub> O <sub>4</sub>	73.96	43.0	0.58	1.66	3.77
Fe <sub>2.67</sub> □ <sub>0.33</sub> O <sub>4</sub>	352	61.5	0.68	2.35	3.95

The larger the particle (grain) size, the greater the flow in the domain movement. The lesser particle size restricts domain movement leading to an increased coercive force (Hc) in the doped spinel compounds.<sup>[45]</sup>

The variation of saturation magnetization (Ms) with different dopants can be estimated by exchange interaction among ions distributed in the octahedral (B) and tetrahedral (A) sites. Neel’s two sublattice models<sup>[46]</sup> are applied to the magnetization at the B sub-lattice is higher than the A sublattice. This model is applied to understand the magnetic behavior of the samples. According to Neel’s two-sublattice model of ferrimagnetism, magnetic moment n<sub>B</sub> is given by n<sub>B</sub> = M<sub>B</sub> – M<sub>A</sub>. Where M<sub>B</sub> and M<sub>A</sub> are the B and A sub-lattice magnetic moments in μ<sub>B</sub>. Using ionic magnetic moments of

Fe<sup>3+</sup>, Zn<sup>2+</sup>, Ni<sup>2+</sup>, Cu<sup>2+</sup> and Co<sup>2+</sup> as 5.92 μ<sub>B</sub>, 0 μ<sub>B</sub>, 2.83 μ<sub>B</sub>, 1.38 μ<sub>B</sub>, and 3.87 μ<sub>B</sub> respectively, and using the above relation, Neel’s magnetic moment has been calculated. The experimental magnetic moment (n<sub>B</sub>) is calculated from the saturation magnetization data using the following relations.

$$n_B = M_w \times M_s / 5585 \tag{6}$$

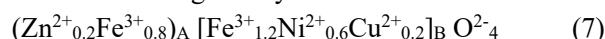
where M<sub>w</sub> is the molecular weight of the doped spinel ferrites, and M<sub>s</sub> is the saturation magnetization in emu/g. The saturation magnetization and the observed and calculated values of magneton numbers are listed in Table 4. It is evident from the table that there is a discrepancy in the observed and calculated values of the magneton number. This suggests that the structure is a non-collinear spin arrangement, i.e., the presence of a small canting of the B-site moment with respect

to the direction of the A-site moment of spinel.<sup>[47]</sup> Furthermore, it is also possible to correlate the observed magnetic moment ( $n_B$ ) to the porosity (P) of these samples (see Table 2). A pore is a sort of void or a gap, and this will break up the magnetic circuit between grains to the grain. If the number of pores is large, this may lead to the net reduction of magnetization in bulk.<sup>[48]</sup> Another reason is that, as discussed in scanning electron microscopy (Fig. 4), the critical grain size decreases due to the displacement of the domain wall added to magnetic losses. This is because the existence of domain walls partly coincides with the grain boundaries. So the increase in grain boundaries with grain size decreases leads to the pinning of domain walls motion.<sup>[49]</sup> As such, it is assumed that magnetic ordering can be broken up easily at nonmagnetic/magnetic (*i.e.*, dopants) grain boundaries, and then there is the presence of short-range magnetic exchange interaction. Therefore, in the range of applied field (H) for hysteresis measurement, the magnetization is not large enough to move the magnetic domain walls, *i.e.*, the contribution of the domain wall displacements in the magnetization process is small which, corresponds to nonmagnetic/magnetic (dopants) pores exist at the grain boundaries. Therefore, the magnetic moment ( $n_B$ ), saturation magnetization ( $M_S$ ) and remanence ratio ( $M_R/M_S$ ) of doped spinel ferrite is less than that of undoped one.

#### (a) $Ni_{0.6}Cu_{0.2}Zn_{0.2}Fe_2O_4$ sample

The variation of magnetization for this sample could be explained based on cation distribution and exchange interaction between iron, zinc, and copper at tetrahedral A and octahedral B sites. K. S. Ramakrishna *et al.*<sup>[50]</sup> in their studies for  $Ni_xCu_{0.1}Zn_{0.9-x}Fe_2O_4$  ferrites ( $X=0.5, 0.6, 0.7$ ) observed as  $Ni^{2+}$  concentration is being increased, their saturation magnetization ( $M_S$ ) and coercive force ( $H_C$ ) increases and then decreases. The highest value of  $M_S = 38.36$  emu/g and  $H_C = 66.77$  Oe is observed for  $x = 0.6$ . They observed that the substitution of  $Cu^{2+}$  in the place of  $Zn^{2+}$  greatly alters the cation distribution forcing more  $Ni^{2+}$  ions into A-site. It is well known that  $Zn^{2+}$  ions strongly prefer A sites (tetrahedral),  $Cu^{2+}$  and  $Ni^{2+}$  ions prefer B sites (octahedral), while  $Fe^{3+}$  ions occupy both A and B sites. The strong preference of  $Zn^{2+}$  ions for A sites displaces some  $Fe^{3+}$  ions from A to B site, which reduces the magnetic moment of the A-site, while the magnetic moment of B-site will increase. When  $Cu^{2+}$  ions are introduced, the  $Fe^{3+}$  ions are left at A-site, being small in number, the A-B interaction experienced by B-site  $Fe^{3+}$  ions decreases. Also, the increased number of  $Fe^{3+}$  ions at the B-site increases the B-B interaction, resulting in spin canting.<sup>[51]</sup> Consequently, the magnetization of B sublattices is decreased. The reason for a decrease in magnetization may also be due to

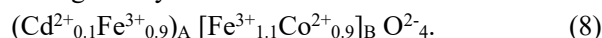
the  $Cu^{2+}$  content, the exchange interaction is weakened, and B spins are no longer held rigidity parallel to the few remaining A spins. The decrease in the B sublattice moment, interpreted as a spin departure from co-linearity, causes the effect known as canting. Therefore, the introduction of  $Ni^{2+}$  and  $Cu^{2+}$  ions, which have a strong preference for the spinel at the B-site and the cation distribution is given by



where the ions enclosed by the round bracket correspond to the tetrahedral A-site and the ions enclosed by the square bracket correspond to the octahedral B-site.

#### (b) $Co_{0.9}Cd_{0.1}Fe_2O_4$ sample

The saturation magnetization of this sample is in full agreement with the Neel theory of ferrimagnetism.<sup>[46]</sup> The introduction of  $Co^{2+}$  ion, which has a strong preference for the spinel B-site, while  $Cd^{2+}$  ion prefers to A-site and the cation distribution is given by



The substitution of paramagnetic  $Co^{2+}$  ions at the B-site, then some  $Fe^{3+}$  ions started to migrate to the A-site hence strengthening the A-B interaction. When the  $Cd^{2+}$  ion is non-magnetic and occupies the  $Fe^{3+}$  site in the A-site sublattice, the magnetic bond  $Fe^{3+}_A - O - Fe^{3+}_B$  decreases, and consequently, the magnetization at the B-site decreases. This decrease in the magnetization of the B-sub lattice, in turn, weakens the magnetic influence of the B-sublattice on the A-sublattice. This decreases the A – B interaction, which results in a decrease in the saturation magnetization.

#### (c) $Al_{0.3}CoFe_{1.7}O_4$ sample

Upon doping of the Fe ions with  $Al^{3+}$  (*i.e.*, non-magnetic ion), changes in the cation distribution take place, which affects the value of the magnetic moment per formula unit. It was found that Fe ions migrate from the octahedral B site to the tetrahedral A site as the concentration of Al ions. So that Fe and Al ions occupy both A and B sites in the spinel structure as

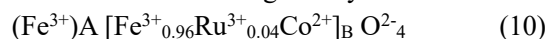


Therefore, the magnetic moment per formula unit decreases as the Al content is due to the doped of the magnetic Fe ion with non-magnetic Al ion and changes in cation distribution. Thus, shifting of magnetic  $Fe^{3+}$  ( $5.92 \mu_B$ ) ion from the sublattice and the doped of the non-magnetic  $Al^{3+}$  (zero  $\mu_B$ ) ions in its place weakens the superexchange interactions. This tends to align neighboring magnetic dipole antiparallely, allowing a decrease in the magnetization due to enhanced spin nonlinearity. Therefore, on  $Al^{3+}$  doping, the saturation magnetization and  $M_R/M_S$  ratio decrease in the present sample

as compared to undoped  $\text{CoFe}_2\text{O}_4$ .<sup>[12]</sup> The more coercive force (see in Table 4) is due to enhanced magnetocrystalline anisotropy induced by the different cation distributions of this sample. P.P. Gauns Desai *et al.*<sup>[52]</sup> observed the saturation magnetization ( $M_s$ ) and Coercive force ( $H_c$ ) decreases with an increase in nonmagnetic  $\text{Al}^{3+}$  concentration for  $\text{Ni}_{0.7}\text{Zn}_{0.3}\text{Fe}_{2-x}\text{Al}_x\text{O}_4$  ferrite system (for  $x = 0.0$  to  $0.3$ ,  $M_s = 65$  to  $47$  emu/g and  $H_c = 80$  to  $30$  Oe respectively). It has been also observed that as the concentration  $\text{Al}^{3+}$  increases, the hysteresis loop becomes very narrow.

#### (d) $\text{CoRu}_{0.04}\text{Fe}_{1.96}\text{O}_4$ sample

The insertion of a small amount of  $\text{Ru}^{3+}$  cations into a cobalt ferrite here may have contributed to magnetization. Hence, in this compound, it may be reasonable that  $\text{Ru}^{3+}$  is considered magnetic at room temperature. Therefore, the effect of ruthenium (Ru) atoms in  $\text{CoFe}_2\text{O}_4$  seems to be similar to the doping of magnetic atoms in the octahedral Fe sites of the spinel lattices. As the net magnetic moments in the ferromagnetic ferrites depends on the number of magnetic ions occupying the tetrahedral (A) and octahedral (B) sites, the reduction of magnetization ( $M_s$ ) as  $\text{Ru}^{3+}$  content. This fact is evident as observed lower saturation magnetization value for Ru-doped cobalt ferrite having smaller crystallite size and average particle size (see Table 2) compound. The  $\text{Ru}^{3+}$  ions have a strong preference for the octahedral lattice (B) site of the spinel. The cation distribution is given by

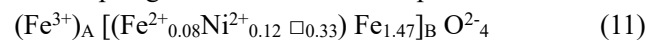


The large coercive force ( $H_c$ ) of this sample may be due to the ruthenium ions ( $\text{Ru}^{3+}$ ) usually having a strong spin-orbit coupling and thereby contribute to the anisotropy of a single-ion source when there located in the B-sites of spinel ferrites. In literature, the magnetization of Ru-doped  $\text{NiFe}_2\text{O}_4$  increased with annealing temperature,<sup>[53]</sup> and showed the narrow area of the hysteresis loop demonstrates soft magnetic nature which depends on the crystallinity dopant and particle size. The observed values of coercivity ( $H_c$ ) = 47.02, 67.92, 99.26 Oe and saturation magnetization ( $M_s$ ) = 3.25, 12.50, 34.92 emu/g increases as the annealed temperature at 300, 600 and 900°C increases respectively. They showed that lower magnetization at 300°C is due to smaller particle size where in a high surface disorder is expected. The coercivity rises with annealing temperatures is due to the grain boundaries can lead to increase pinning sites for spins and also, increases the strong exchange coupling as well growth of anisotropic properties.

#### (e) $\text{Fe}_{2.55}\text{Ni}_{0.12}\square_{0.33}\text{O}_4$ sample

The hysteresis loops of the as-synthesized Ni-doped gamma ferric oxide,  $\text{Fe}_{2.55}\text{Ni}_{0.12}\square_{0.33}\text{O}_4$  sample at room temperature (300 K) is shown in Fig. 11 (a). This result indicates that all

particles are likely to have ferromagnetic properties at room temperature since the remanence ratio of the particles is equal to 0.19 and the coercivity is 73.96 Oe in the absence of an external magnetic field. It can be seen that the magnetic hysteresis loop obtained from the magnetization cycle is considerably small. The constant value or level in the horizontal region of the magnetization curve in the magnetic field, which seems to some extent to be out of  $\pm 50$  Koe range, may suggest that the nanoparticles have attained their saturated magnetization level, *i.e.*, 40 emu/g. This value is less than undoped gamma ferric oxide (see Table 4). Referring to the average grain size of the nanoparticles (20 nm) and the magnetic hysteresis loop, it could be claimed that magnetic nanoparticles are not superparamagnetic. Similar magnetization have has been observed in cobalt and gadolinium doped  $\text{Fe}_{2.67}\square_{0.33}\text{O}_4$  (*i.e.*  $\gamma\text{-Fe}_2\text{O}_3$ ) spinel ferrite.<sup>[54]</sup> They reported that the saturation magnetization ( $M_s$ ) = 56.8 and 46.0 emu/g, coercive force ( $H_c$ ) = 387 and 346 Oe respectively for 1 wt% cobalt and gadolinium-doped gamma ferric oxide. These samples have been found to be single domains. The magnetization of this sample at a temperature of 2K is presented in Fig. 11 (b). The particles do have adequate thermal energy to attain complete thermal equilibrium with the applied field during the measurement time, and hence, hysteresis appears. It may be noted from Fig. 11 (b) that the hysteresis loop is open. The open hysteresis loop at 50 KOe and the ZFC/FC separation (Fig. 11 (c)) suggest high field irreversibility. In a manner similar to 300 K (*i.e.*, room temperature), the saturation magnetization of  $\text{Fe}_{2.55}\text{Ni}_{0.12}\square_{0.33}\text{O}_4$  obtained at 2 K was estimated and found a good agreement with each other. This is indicative of the presence of ferromagnetic nanosized material. The ZFC – FC magnetization process at 100 Oe exhibit the typical features of an assembly of magnetic particles with a distribution of blocking temperature (see Fig. 11 (c)). In this sample, the ZFC and FC magnetization curves (Fig. 11 (c)) only collapse at the highest temperature measured (300 K), thus indicating that the blocking temperature is above room temperature. The observed irreversibility of the ZFC-FC curve indicative of ferromagnetism exists in this sample. According to Neel's two sublattice model of ferrimagnetism,<sup>[46]</sup> the cation distribution for nickel-doped gamma ferric oxide sample can be written as



Although there is not much change in the bonding of iron atoms at the A-site, some change in bonding does take place at the octahedral B-site to nickel concentration. Therefore, nickel enters Fe vacant sites at the B-site of the spinel.

A thermogravimetric (TGA) method can be applied to the evaluation of the cationic *i.e.* Fe vacancy, ( $\delta$ ) in spinel ferrites.

This method correlates the Fe vacancy ( $\delta$ ) with the weight change due to oxygen evolution through the charge and mass balance in the spinel ferrite. From this data, the Fe vacancy ( $\delta$ ) at room temperature was calculated by using the following expression.<sup>[55]</sup>

$$\delta = (\alpha - 3\theta) / m \quad (12)$$

Where  $\delta$  = Fe (*i.e.* cationic) vacancy,  $\alpha$  = initial mass ( $m_i$ ) of the sample taken in mg,  $\theta$  = molar fraction *i.e.* a certain amount of mass loss in mg,  $\Delta m = m_i - m_f$  (where  $m_i$  and  $m_f$  are the initial and final mass of the sample) and  $m = (4 + 3\alpha - \theta)$  called the cationic coefficient. These authors<sup>[55]</sup> also discussed the change in Fe vacancy ( $\delta$ ) due to atmosphere changes are much more significant and these changes can be correlated to changes in the spinel ferrite magnetic properties. Further, they suggested that the values obtained for  $\delta$  will not be altered by the presence of some electron hopping between  $\text{Fe}^{2+}$  and  $\text{Fe}^{3+}$  cations.

#### 4. Conclusions

Five nanosized doped spinel ferrites such as  $\text{Ni}_{0.6}\text{Cu}_{0.2}\text{Zn}_{0.2}\text{Fe}_2\text{O}_4$ ,  $\text{Co}_{0.9}\text{Cd}_{0.1}\text{Fe}_2\text{O}_4$ ,  $\text{Al}_{0.3}\text{CoFe}_{1.7}\text{O}_4$ ,  $\text{CoRu}_{0.04}\text{Fe}_{1.96}\text{O}_4$ , and  $\text{Fe}_{2.55}\text{Ni}_{0.12}\text{Co}_{0.33}\text{O}_4$  samples are synthesized by soft chemical routes. The X-ray diffraction of these samples possesses a single-phase spinel structure with a slightly enlarged lattice constant as compared to respective undoped spinel ferrite samples. SEM and TEM images along with particle size distribution histograms confirmed the nano-size particle for these spinel ferrites. The electrical conductivity, Seebeck voltage and Hall effect measurements for all samples showed an n-type semiconductor. All doped samples show typical hysteresis behavior with a decrease in saturation magnetization ( $M_s$ ), and the remanence ratio ( $M_R / M_s$ ) due to the weak superexchange interaction and an increase in coercivity ( $H_c$ ) as compared to respective undoped spinel ferrites. The observed and calculated values of magneton number ( $n_B$ ) for all samples showed a significant canting spin exists at the octahedral B-site. A high value of coercivity ( $H_c$ ) makes all synthesized materials except  $\text{CoRu}_{0.04}\text{Fe}_{1.96}\text{O}_4$  sample is required for the applications in longitudinal recording media. While  $\text{CoRu}_{0.04}\text{Fe}_{1.96}\text{O}_4$  sample will be suitable for application in perpendicular high-density recording media.

#### Acknowledgments

The authors thank the staff from TIFR, Mumbai for their technical support during the SEM-EDS and magnetization measurement experiment. They also thank DST-FIST Delhi, the staff from SAIF laboratories IIT Mumbai, for ICPES and TEM-SAED experiment.

#### Conflict of Interest

There is no conflict of interest.

#### Supporting Information

Applicable.

#### References

- [1] S. Laurent, D. Forge, M. Port, A. Roch, C. Robic, L. Vander Elst, R. N. Muller, Magnetic iron oxide nanoparticles: synthesis, stabilization, vectorization, physicochemical characterizations, and biological applications, *Chemical Reviews*, 2008, **108**, 2064-2110, doi: 10.1021/cr068445e.
- [2] A Goldman, Modern Ferrite Technology, Springer-Verlay, PA, 2006 Pittsburgh.
- [3] S. Chakrabarty, M. Pal, A. Dutta, Structural, optical and electrical properties of chemically derived nickel substituted zinc ferrite nanocrystals, *Materials Chemistry and Physics*, 2015, **153**, 221-228, doi: 10.1016/j.matchemphys.2015.01.006.
- [4] K. E. Sickafus, J. M. Wills and N. W. Grimes, Structure of Spinel, *Journal of American Ceramic Society*, 1999, **82**, 3279-3292, doi: 10.1111/j.1151-2916.1999.tb02241.x.
- [5] D. V. Kurmude, R. S. Barkule, A. V. Raut, D. R. Shengule, K. M. Jadhav, X-ray diffraction and cation distribution studies in zinc-substituted nickel ferrite nanoparticles, *Journal of Superconductivity and Novel Magnetism*, 2014, **27**, 547-553, doi: 10.1007/s10948-013-2305-2.
- [6] A. T. Raghavender, R. G. Kulkarni, K. M. Jadhav, Magnetic Properties of Nanocrystalline Al Doped Nickel Ferrite Synthesized by the Sol-Gel Method, *Chinese Journal of Physics*, 2008, **46**, 366-375, doi: 10.6122/CJP.
- [7] W. Ying, K. X. Yu, Y. Xiong, W. Hui, EPR investigation of the site symmetry of  $\text{Fe}^{3+}$  ions in the spinel crystals, *Physica B: Condensed Matter*, 2006, **381**, 260-264, doi: 10.1016/j.physb.2006.01.495.
- [8] H. Bordeneuve, C. Tenailleau, S. Guillemin-Fritsch, R. Smit, E. Suard, A. Rousset, Structural variations and cation distributions in  $\text{Mn}_{3-x}\text{Co}_x\text{O}_4$  ( $0 \leq x \leq 3$ ) dense ceramics using neutron diffraction data, *Solid State Sciences*, 2010, **12**, 379-386, doi: 10.1016/j.solidstatesciences.2009.11.018.
- [9] K. Haneda, A. H. Morish, Noncollinear magnetic structure of  $\text{CoFe}_2\text{O}_4$  small particles, *Journal of Applied Physics*, 1988, **63**, 4258-4260, doi: 10.1063/1.340197.
- [10] L. Lin, K. H. Hsu, J. G. Lin, Doping effects on the magnetic resonance of  $\text{ZnFe}_2\text{O}_4$  and  $\text{NiFe}_2\text{O}_4$ , *Journal of Magnetism and Magnetic Materials*, 2006, **304**, 467-469, doi: 10.1016/j.jmmm.2006.02.069.
- [11] V. Rao, A. L. Shashimohan, A. B. Biswas, Studies on the formation of  $-\text{Fe}_2\text{O}_3$  (maghemite) by thermal decomposition of ferrous oxalate dihydrate, *Journal of Materials Science*, 1974, **9**, 430-433, doi: 10.1007/bf00737843.
- [12] A. K. Nikumbh, A. V. Nagawade, V. B. Tadke, P. P. Bakare, Electrical, magnetic and Mössbauer properties of cadmium - cobalt ferrites prepared by the tartarate precursor method, *Journal of Materials Science*, 2001, **36**, 653-662, doi:

- 10.1023/A:1004872405266.
- [13] H. Kaur, A. Singh, V. Kumar, D. Singh Ahlawat, Structural, thermal and magnetic investigations of cobalt ferrite doped with  $Zn^{2+}$  and  $Cd^{2+}$  synthesized by auto combustion method, *Journal of Magnetism and Magnetic Materials*, 2019, **474**, 505-511, doi: 10.1016/j.jmmm.2018.11.010.
- [14] A. K. Nikumbh, R. A. Pawar, D. V. Nighot, G. S. Gugale, M. D. Sangale, M. B. Khanvilkar, A. V. Nagawade, Structural, electrical, magnetic and dielectric properties of rare-earth substituted cobalt ferrites nanoparticles synthesized by the coprecipitation method, *Journal of Magnetism and Magnetic Materials*, 2014, **355**, 201-209, doi: 10.1016/j.jmmm.2013.11.052.
- [15] L. Kumar, M. Kar, Influence of  $Al^{3+}$  ion concentration on the crystal structure and magnetic anisotropy of nanocrystalline spinel cobalt ferrite, *Journal of Magnetism and Magnetic Materials*, 2011, **323**, 2042-2048, doi: 10.1016/j.jmmm.2011.03.010.
- [16] A. Ghasemi, E. Ghasemi, E. Paimozd, Influence of copper cations on the magnetic properties of NiCuZn ferrite nanoparticles, *Journal of Magnetism and Magnetic Materials*, 2011, **323**, 1541-1545, doi: 10.1016/j.jmmm.2011.01.014.
- [17] A. K. Nikumbh, A. V. Nagawade, G. S. Gugale, M. G. Chaskar, P. P. Bakare, The formation, structural, electrical, magnetic and Mössbauer properties of ferrispinel,  $Cd_{1-x}Ni_xFe_2O_4$ , *Journal of Materials Science*, 2002, **37**, 637-647, doi: 10.1023/a: 1013790129045.
- [18] A. Tomitaka, T. Koshi, S. Hatsugai, T. Yanmada, Y. Takemura, Magnetic characterization of surface-coated magnetic nanoparticles for biomedical application, *Journal of Magnetism and Magnetic Materials*, 2011, **323**, 1398-1403, doi: 10.1016/j.jmmm.2010.11.054.
- [19] I. Desai, M. N. Nadagouda, M. Elovitz, M. Mill, B. Boulanger, Synthesis and characterization of magnetic manganese ferrites, *Materials Science for Energy Technologies*, 2019, **2**, 150-160, doi: 10.1016/j.mset.2019.01.009.
- [20] S. Chakrabarti, S. K. Mandal, S. Chaudhari, Cobalt doped  $\gamma$ - $Fe_2O_3$  nanoparticles: synthesis and magnetic properties, *Nanotechnology*, 2005, **16**, 506-511, doi: 10.1088/0957-4484/16/4/029.
- [21] S. Hamdy, M. B. Mohamed, S. S. Ata-Allah, Effect of Zn, Ga and Gd doping on structural and magnetic properties of nanonickel ferrite prepared by two different methods, *Journal of Superconductivity and Novel Magnetism*, 2019, **32**, 115, doi: 10.1007/s10948-018-4893-3.
- [22] R. Giovanoli, R. Brutsch, Dehydration of gamma- $FeOOH$ -direct observation of mechanism, *Chimia*, 1974, **28**, 188-191.
- [23] M. B. Khanvilkar, A. K. Nikumbh, R. A. Pawar, N. J. Karale, D. V. Nighot, G. S. Gugale, Synthesis and physicochemical properties of doped nano oxides-dilute magnetic semiconductors, *Journal of Materials Science: Materials in Electronics*, 2019, **30**, 13217-13222, doi: 10.1007/s10854-019-01685-3.
- [24] J. R. Allan, G. M. Baillie, N. D. Baird, The spectral and magnetic properties of some chloro and bromo transition metal complexes of isonicotinic acid, *Journal of Coordination Chemistry*, 1980, **10**, 171-175, doi: 10.1080/00958978008081012.
- [25] J. R. Allan, A. D. Paston, K. Turvey, H. J. Bowley, D. L. Gerrad, Thermal and electrical studies on pyrazine-2,3-dicarboxylic acid compounds of manganese(II), cobalt(II), nickel(II), copper(II) and zinc(II), *Thermochim Acta*, 1988, **124**, 345-357, doi: 10.1016/0040-6031(88)87037-0.
- [26] M. B. Khanvilkar, A. K. Nikumbh, R. A. Pawar, N. J. Karale, D. V. Nighot, R. C. Ambare, P. A. Nagawade, M. D. Sangale, G. S. Gugale, S. B. Misal, Preparation and Characterization of Nanosized Substituted Perovskite Compounds with Orthorhombic Structure, *Physics and Chemistry of Solid State*, 2021, **22**, 664-686. doi: 10.15330/pcss.22.4.664-686.
- [27] A. A. Ghani, A. A. Sattar, Composition dependence of magnetization in  $Co_{1-x}Cd_xFe_2O_4$  ferrites, *Journal of Magnetism and Magnetic Materials*, 1991, **97**, 141-146 doi: 10.1016/0304-8853(91)90173-8.
- [28] M. A. Ahmed, M. M. EL-Sayyed, Magnetic characterization and thermoelectric power of  $Ni_{1-y}Zn_y Cu_{0.3}Fe_{1.7}O_4$ ;  $0.0 \leq y \leq 0.6$ , *Journal of Magnetism and Magnetic Materials*, 2007, **308**, 40-45, doi: 10.1016/j.jmmm.2006.04.034.
- [29] T. Inoue, D. Kagaku, History of ECSJ Awards and Introduction of Award Winners in 2021, *Electrochemistry*, 1955, **23**, 24, doi: 10.5796/electrochemistry 21-00102.
- [30] J. Bernal, D. Dasgupta, A. Mackay, Oriented transformations in iron oxides and hydroxides, *Nature (London)*, 1957, **180**, 645-647, doi: 10.1038/180645a0.
- [31] A. M. EL-Sayyed, Influence of zinc content on some properties of Ni-Zn ferrites, *Ceramics International*, 2002, **28**, 363-367, doi: 10.1016/S0272-8842(01)00103-1.
- [32] B. D. Cullity, Elements of X-ray diffraction and Addison Wesley Publication Company Inc. Indiana, U.S.A. 1959.
- [33] T. Abbas, M. U. Islam, M. A. Chaudhary, Study of sintering behavior and electrical properties of Cu-Zn-Fe-O system *Modern Physics Letters B*, 1995, **22**, 1419-1426, doi: 10.1142/S0217984995001418.
- [34] P. Singh, V. K. babbar, A. Razdan, S. L. Srivastava, V. K. Agrawal, T. C. Goel, Dielectric constant, magnetic permeability and microwave absorption studies of hot-pressed Ba-CoTi hexaferrite composites in X-band, *Journal of Materials Science*, 2006, **41**, 7190-7196, doi: 10.1007/s10853-006-0921-y.
- [35] K. Ravichandan, D. Nedumaran, *International Journal of Mechanical and Materials Engineering*, 2011, **4**, 25-30, doi: ISSN-2198-2791(electronic).
- [36] O. S. Josyulu, J. Sobhanadri, The far-infrared spectra of some mixed cobalt zinc and magnesium zinc ferrites, *Physica Status Solidi (a)*, 1981, **65**, 479-483, doi: 10.1002/pssa.2210650209.
- [37] B. J. Evans, O. K. Hang Nam, Collective electron states in  $Zn_xFe_{3-x}O_4$  and  $Cd_xFe_{3-x}O_4$  for  $0 \leq x \leq 0.3$ , *Physica B+C*, 1977, **86-88**, 931-933, doi: 10.1016/0378-4363 (77) 90747-1.
- [38] M. Mogensen, N. M. Sammes, G. A. Tom, Effect of surface modifications on the layered solid solution cathodes  $(1 - z) Li[Li_{1/3}Mn_{2/3}]O_2 - (z) Li[Mn_{0.5} - yNi_{0.5} - yCo^{2y}]O_2$ , *Solid State Ionics*, 2009, **180**, 63-72, doi: 10.1016/j.ssi.2008.11.002.

- [39] E. J. W. Verway, *Semiconducting Materials*, (H. K. Henisch, Edition) Butterworths, 1951, page 151, London.
- [40] A.M. Abo El Ata, S.M. Attia, T.M. Meaz, AC conductivity and dielectric behavior of  $\text{CoAl}_x\text{Fe}_{2-x}\text{O}_4$ , *Solid State Sciences*, 2004, **6**, 61-69, doi: 10.1016/j.solidstatesciences.2003.10.006.
- [41] M. I. Iqbal, R. A. Khan, S. Takeda, S. M. Zukami, T. Miyazaki, W-type hexaferrite nanoparticles: A consideration for microwave attenuation at wide frequency band of 0.5–10 GHz, *Journal of Alloys and Compounds*, 2011, **509**, 7618-7624, doi: 10.1016/j.jallcom.2011.04.103.
- [42] J. Gao, Y. Cui, Z. Yang, The magnetic properties of  $\text{Ni}_x\text{Zn}_{1-x}\text{Fe}_2\text{O}_4$  films fabricated by alternative sputtering technology, *Materials Science and Engineering: B*, 2004, **110**, 111-114, doi: 10.1016/j.mseb.2003.10.111.
- [43] Y. Li, R. Liu, Z. Zhang, C. Xiang, Synthesis and characterization of nanocrystalline  $\text{BaF}_{0.6}\text{Co}_{0.8}\text{Ti}_{0.8}\text{Mn}_{0.8}\text{O}_{19}$  particles, *Materials Chemistry and Physics*, 2000, **64**, 256-259, doi: 10.1016/S0254-0584(99)00218-7.
- [44] H. N. Chaudhari, P. N. Dhruv, C. Singh, S. Singh Meena, S. Kavita, R. B. Jotania, Effect of heating temperature on structural, magnetic, and dielectric properties of Magnesium ferrites prepared in the presence of Solanum Lycopersicum fruit extract, *Journal of Materials Science: Materials in Electronics*, 2020, **31**, 18445, doi:10.1007/s10854-020-04389-1.
- [45] C. N. Chinnasamy, B. Jeyadevan, K. Shinoda, K. Tohji, D. J. Djayaprawira, M. Takahashi, R. Justin Joseyphus, A. Narayanasamy, Unusually high coercivity and critical single-domain size of nearly monodispersed  $\text{CoFe}_2\text{O}_4$  Nanoparticles, *Applied Physics Letters*, 2003, **83**, 2862, doi: 10.1063/1.1616655.
- [46] M. Louis Neel, Magnetic properties of ferrites; ferrimagnetism and antiferromagnetism, *Annals of Physics*, 1948, **12**, 137-198, ISSN: 003-4169, eISSN:1286-4838.
- [47] Y. Yafet, C. Kittel, Antiferromagnetic Arrangements in Ferrites, *Physics Review*, 1952, **87**, 290-294, doi: 10.1103/PhysRev.87.290.
- [48] H. Rikukawa, Relationship between microstructures and magnetic properties of ferrites containing closed pores, *IEEE Transactions on Magnetics*, 1982, **18**, 1535-1537, doi: 10.1109/TMAG.1982.1062065.
- [49] S. B. Ren, C. J. Lu, H. M. Shen, Y. N. Wang, In situ study of the evolution of domain structure in free-standing polycrystalline  $\text{PbTiO}_3$  thin films under external stress, *Physical Review B*, 1997, **55**, 3485-3489, doi: 10.1103/PhysRevB.55.3485.
- [50] K. S. Ramakrishna, C. Srinivas, S. S. Meena, B. V. Tirupanyam, P. Bhatt, S. M. Yusuf, C. L. Prajapat, D. M. Potukuchi, D. L. Sastry, *Ceramics International*, 2017, **43**, 7984-7991, doi: 10.1016/j.ceramint.2017.03.078.
- [51] S. E. Shrisath, B. G. Toksha, R.H. Kadam, S. M. Patange, D.R. Mane, G. S. Jangam, A. Ghasemi, Doping effect of  $\text{Mn}^{2+}$  on the magnetic behavior in Ni–Zn ferrite nanoparticles prepared by sol–gel auto-combustion, *Journal of Physics and Chemistry of Solids*, 2010, **71**, 1669-1675. doi: 10.1016/j.jpics.2010.08.016.
- [52] P. P. Gauns Dessai, S. S. Meena, V. M. S. Verenkar, Influence of addition of  $\text{Al}^{3+}$  on the structural and solid state properties of nanosized Ni–Zn ferrites synthesized using malic acid as a novel fuel, *Journal of Alloys and Compounds*, 2020, **842**, 155855, doi: 10.1016/j.jallcom.2020.155855.
- [53] V. Manikandan, A. Mizzaei, S. Vigneselvan, S. Kavita, R.S. Mane, S. S. Kim, J. Chandrasekaran, Role of ruthenium in the dielectric, magnetic properties of nickel ferrite ( $\text{Ru–NiFe}_2\text{O}_4$ ) Nanoparticles and their application in hydrogen sensors, *ACS Omega*, 2019, **4**, 12919-12926, doi:10.1021/acsomega.9b01562.
- [54] A. K. Nikumbh, Magnetic properties and Mössbauer spectra of gamma ferric oxide and doped gamma ferric oxide, *Journal of Materials Science*, 1990, **25**, 3773-3779, doi:10.1007/BF00575417.
- [55] A. Gonzalez Arias, A. delCueto, J. M. Munoz, C. de Francisco, Deposition of nanostructured CdS thin films by thermal evaporation method: effect of substrate temperature, *Materials*, 1998, **37**, 187-191, doi: 10.1016/S0167-577X(98)00089-5.

### Author Information



**Mahesh B. Khanvilkar** is working as Professor of Chemistry at K. M. C. College, Khopoli since 1988. He has completed his Ph.D. from Savitribai Phule Pune University, Pune in 2014. He is working as ex-Incharge Principal and Head, in the same institute. He is working in the area of Material science, heterogeneous catalysis, nanomaterials etc. He has published 12 research papers in various reputed international journals and published 02 book chapters. He has been awarded the 'Best NSS Programmer Officer' by University of Mumbai, Mumbai, India in 2006 for his excellent contribution in extension activities.



**Arvind K. Nikumbh** is an ex-Professor of Inorganic Chemistry in the Department of Chemistry, Savitribai Phule Pune University (Formerly University of Pune) Pune-411007, India. He received his master's degree in Inorganic Chemistry in 1976 and his Ph. D in 1982 from the Department of Chemistry, University of Pune. During 1986-1988 he was a postdoctoral fellow at Karsruhe, Germany under DAAD Fellowship. His current research interest include electrothermal analysis of metal (II) dicarboxylates, slip casting of ceramic oxide, nanomaterials such as mixed ferrites, substituted perovskite and pyrochlore oxides and photocatalysis. He has several publications in peer review International journals. He is also a reviewer of many International journals of his research area.



**Ramdas A. Pawar** is Professor of Chemistry working in the Department of Chemistry, Prof. Ramkrishna More ACS College, Akurdi, Pune. He received master degree in Inorganic Chemistry in 1993 and his Ph. D. in 2006 from Department of Chemistry, Savitribai Phule Pune University, Pune. His current research interest includes Nanomaterials, heterogeneous catalysis and sensors. He has published several research papers in the journals of international repute with total citation-348, with h-index-08 and i-10 index-07. Two students completed their Ph. D. research under his supervision. He is able to grab research funding of about 6.5 lakh from UGC and BCUD, SPPU, Pune. He has been awarded the 'NSS Best Programmer Officer' by Mahajana Education Society, Mysore, and Karnataka, India in 2003 for his excellent contribution in extension activities.



**Neeta J. Karale** is working as an Assistant Professor at Fergusson College, Pune since 2006. She has completed her Ph.D. at Savitribai Phule Pune University, Pune in 2016. Her area of research is in the field of Material Science. She has published 09 research papers in various Journals.



**Pratik A. Nagwade** has completed his Ph.D. degree in the year 2017 from Savitribai Phule Pune University, Pune in the area of materials science. Presently he is working as Assistant Professor and Ph.D. guide in Chemistry at Shri Anand College, Pathardi, Dist. Ahmednagar. He has published 12 research papers in various journals.



**Deepak V. Nighot** is presently working as Associate Professor in the Department of Engineering Science, AISSMS College of Engineering, Pune since 1999. He has received his Ph. D. from Savitribai Phule Pune University, Pune (SPPU). His research interest is in material science particularly electrothermal analysis, synthesis and characterization of the mixed metal dicarboxylato complexes route to convert novel semiconductor nanomaterials. He has received Ph. D. guide recognition in Chemistry from SPPU, Pune. He has published 12 research articles in the reputed international journals and published 4 book chapters.



**Gulab S. Gugale** received his master degree and Ph.D. in Inorganic Chemistry from Savitribai Phule Pune University (earlier University of Pune), Pune, India. He is working as Head, Department of chemistry in The Poona Gujrati Kelvani

Mandal's Haribhai V. Desai College, Pune from 1993. Now he is working as Professor in the same institute. He is working in the area of Material science, organic and inorganic semiconductors, photocatalysis, spinel ferrite nanomaterials etc. More than 20 research papers are in his credit. He has published 78 book chapters in the Chemistry subject.



**Mohan D. Sangale** is presently working as a Professor in Chemistry at S.S.G.M. College Kopargaon District Ahmednagar (Maharashtra) India. He is research supervisor in S. P. P. University, Pune. His area of interest are Material Science. He has Published 25 research Papers and presented more than 50 papers in national and international conferences (that is Germany, Bangkok, Thailand). He has published 10 book chapters in Chemistry subject.



**Sham B. Misal** received his master's degree in Inorganic Chemistry, M. Phil. Degree in Chemistry and Ph.D. degree in Chemistry from the Savitribai Phule Pune University, Pune. The title of his thesis at M. Phil. degree is Synthesis and Characterization of Substituted M-type Hexaferrite by Tartrate Coprecipitation. The title of his Ph.D. thesis is Preparation and Properties of Substituted Hard and Soft Ferrites. He has published several research papers in peer-reviewed international journals. Presently he is working as an Assistant Professor in Rayat Shikshan Sanstha's Annasaheb Awate Arts, Commerce & Hutatma Babu Genu Science College, Manchar, Pune. He received Ph. D. guide recognition from Savitribai Phule Pune University, Pune. His area of research is mixed metal oxides, ferrite nanomaterials. Presently he is working on Lanthanum substituted mixed metal oxides.



**Sharad P. Panchgalle**, did his post-graduation in Chemistry from Swami Ramanand Teerth Marathwada University, Nanded in 2001 with second rank in merit order. He received Ph. D. degree from Savitribai Phule Pune University in 2010. In 2010-11, he had worked as post-doctoral researcher with Prof. Alfred Hassner at Bar-Ilan University, Ramat Gan, Israel. Presently, he is working as Assistant Professor in Department of Chemistry, KMC College Khopoli (affiliated to University of Mumbai) since 2012. His area of interest is organocatalysis, total synthesis, chemical biology, heterocycle synthesis through multi-component reactions, etc.

**Publisher's Note:** Engineered Science Publisher remains neutral with regard to jurisdictional claims in published maps and institutional affiliations.